International Journal of Concrete Structures and Materials

RESEARCH Open Access

Investigation on Effects of Particle Internal Pores on Ionic Diffusivity of Hydrated Tricalcium Silicate Paste using a Hydration-Diffusion Simulation Method

Xin Wang[1,2], Dejian Shen[1,2*], Sijie Tao[1,2] and Ruixin Liu[1,2]

Abstract

The long-term durability of concrete is essential for sustainable construction and reducing carbon emissions. A key factor affecting durability is the ingress of hazardous substances, making the understanding of ionic diffusion in concrete crucial. While ionic diffusion is significantly affected by the microstructure of cement paste, existing diffusion models often oversimplify this microstructure by neglecting particle internal pores (PIPs). This simplification can lead to inaccuracies in predicting ionic diffusivity and, consequently, the long-term performance of concrete structures. This study addresses this critical gap by developing a hydration-diffusion simulation method to investigate the effects of PIPs on ionic diffusion in hydrated tricalcium silicate (C_3S), a primary constituent of cement clinker. Our simulations revealed that: (1) the effects of PIP size distribution and particle porosity (PP) on ionic diffusion depended on the water content, water-to-solid ratio, solid C_3S content, and hydration age; (2) at early ages, in hydration systems with a fixed C_3S content or water-to-solid ratio, higher PP would result in lower ionic diffusivity in hydrated C_3S paste. However, contrasting conclusions emerged under conditions of fixed water content; (3) the effects of PIPs on the ionic diffusion in hydrated C_3S also varied with hydration age and water-to-solid ratio.

Keywords Tricalcium silicate, Cement hydration, Particle internal pores, Ionic diffusivity, Particle porosity

1 Introduction

Concrete is one of the most extensively utilized construction materials globally, owing to its remarkable versatility and strength. However, prolonged exposure of reinforced concrete structures to corrosive environments leads to property degradation, primarily induced by chloride ingress (Mien et al., 2011; Patel et al., 2018; Poupard et al., 2004; Tang, 1996, 1999a, 1999b; Wang et al., 2012) and sulfate attack (Bakharev et al., 2002; Gospodinov et al., 2007; Ismail et al., 2013; Neville, 2004). Reinforced concrete structures failing to meet specified property criteria necessitate restoration to extend their service life. However, this restoration process results in a substantial release of carbon dioxide, leading to both considerable economic losses and environmental pollution (ASCE, 2019; Cheng, 2022; Shi et al., 2012). A recent report has shown that doubling the service life of concrete could reduce carbon emissions by 11.3% (Thepaper, 2022). Presently, the service life of concrete structures can be improved by (1) applying corrosion-resistant materials to the concrete surface; (2) hindering the transportation of hazardous substances within the concrete; (3) controlling the critical chloride ionic concentration of steel bars; and

Journal information: ISSN 1976-0485 / eISSN 2234-1315.

*Correspondence:
Dejian Shen
shendjn@163.com
[1] College of Civil and Transportation Engineering, Hohai University, No. 1, Xikang Road, Nanjing 210098, China
[2] Jiangsu Engineering Research Center of Crack Control in Concrete, No. 1, Xikang Road, Nanjing 210098, China

(4) non-destructive repair of corroded steel bars. Among these strategies, hindering the transportation of hazardous ions in concrete is the most frequently employed one (C. Liu & Zhang, 2021; Liu et al., 2020a, 2020b; Patel et al., 2016; Wilson et al., 2021; Zhang et al., 2017). Therefore, for concrete exposed to corrosive environments, investigating ionic diffusivity of concrete contributes to improving its durability and service life, which further helps to reduce carbon emissions and improve sustainable development in the construction industry.

The microstructure is crucial to calculate the ionic diffusivity of cement paste which is the main component of concrete (Barnes & Bensted, 2003; Mehta & Monteiro, 2007; Zhu et al., 2021). The microstructure of cement paste is largely determined by its hydration process. Upon contact with water, cement particles undergo hydrolysis reactions, releasing ions into the pore solution. As hydration progresses, the ionic concentration of aqueous species continues to rise. Upon reaching a saturation point, hydration products begin to precipitate, with crystal growth occurring on the particle surfaces or at random locations within the pore solution (Kurdowski, 2014; Scrivener et al., 2015, 2019; Shen et al., 2022). Hence, the initial microstructure of the particles plays a crucial role in cement hydration. The results in (Liu et al., 2018) demonstrate that irregular cement particles can reduce pore size and increase pore tortuosity. These alterations in pore structure subsequently affect the transport of ions within the microstructures. Additionally, the results in (L. Liu et al., 2020a, 2020b; Zhu et al., 2020) indicate a positive correlation between particle sphericity and hydration kinetics. The decreased particle sphericity increases the specific surface area of reactants, thereby improving the contact area between water and reactants (Liu et al., 2018). This, in turn, accelerates the hydration rate and contributes to microstructural development. Therefore, the available pathways for ionic diffusion are reduced, ultimately leading to a decrease in ionic diffusivity. These studies indicate that the ionic diffusivity of cement paste can be significantly affected by the initial microstructure of cement paste. Thus, the investigation on the microstructure of hydrated cement and its relationship with ionic diffusivity is necessary.

Most studies focus on the effects of external microstructure of particles on ionic diffusion (L. Liu et al., 2020a, 2020b; Zhu et al., 2021). However, relatively little attention is paid to the internal microstructure of particles. Previous studies (Chen et al., 2019; Yang et al., 2018) has revealed that the interior of cement particles may not be completely solid. The results in (Yang et al., 2018) have identified the presence of open and sealed pores within hydration particles using a serial block-face scanning electron microscopy (SBFSEM) system. These open and sealed pores are referred to as the particle internal pores (PIPs) (Wang et al., 2021). The results in (Wang et al., 2021) indicate that PIPs can significantly influence the hydration rate, particularly during the acceleration period. The results in (Chen et al., 2019) indicate that the sealed pores gradually transform into open pores during cement hydration, leading to changes in the spatial distribution of hydration products. Therefore, within the hydrated cement paste, PIPs may indirectly affect ionic diffusion. However, the study in this domain is still relatively limited. The investigation on the relationship between internal microstructure of particles (i.e., PIP) and ionic diffusion was necessary.

The tricalcium silicate (C_3S) constitutes a significant proportion, ranging from 50 to 70% (Taylor, 1997), of cement clinker, making it the primary component that governs the properties of cement paste (Do et al., 2015). Consequently, C_3S has been widely utilized as a material model to explore the hydration mechanisms of cement (Bellmann et al., 2012; Biernacki & Gottapu, 2015; Bullard, 2008; Shen et al., 2022; Wu et al., 2020a, 2020b; Xie & Biernacki, 2011). Despite its significance, there has been limited research on the ionic diffusion of C_3S paste, with most studies focusing on the diffusion behavior in cement, mortar, and concrete. The manufacturing process of cement particles closely resembles the synthesis of pure C_3S, involving processes such as firing and grinding (Costoya Fernández, 2008; Taylor, 1997). The PIP in C_3S particles has been identified by the SBFSEM system (Yang et al., 2018), suggesting that PIPs may also be present in cement particles. Therefore, the investigation on hydrated C_3S would contribute to comprehending effects of PIP on ionic diffusion in hydrated cement system.

The literature describes numerous simulation methods designed to predict ionic diffusivity in cement paste. These methods can be broadly grouped into three categories. (Patel et al., 2016): empirical methods, effective medium theory methods, and microstructure-based methods. The empirical method establishes a relationship between the diffusion coefficient and influencing factors (such as porosity and w/c ratio) by fitting empirical formulas to experimental data (Oh & Jang, 2004). This method provides a simplified representation of the complex diffusion process in cement paste based on empirical correlations. The effective medium theory method predicts ionic diffusion by considering serial or parallel geometrical configurations (Bejaoui & Bary, 2007). It treats the cement paste as a composite material and uses effective medium theories to estimate the diffusion behavior based on the properties of the individual components and their spatial arrangement. The microstructure-based method leverages hydration models to generate virtual microstructures of hydrated

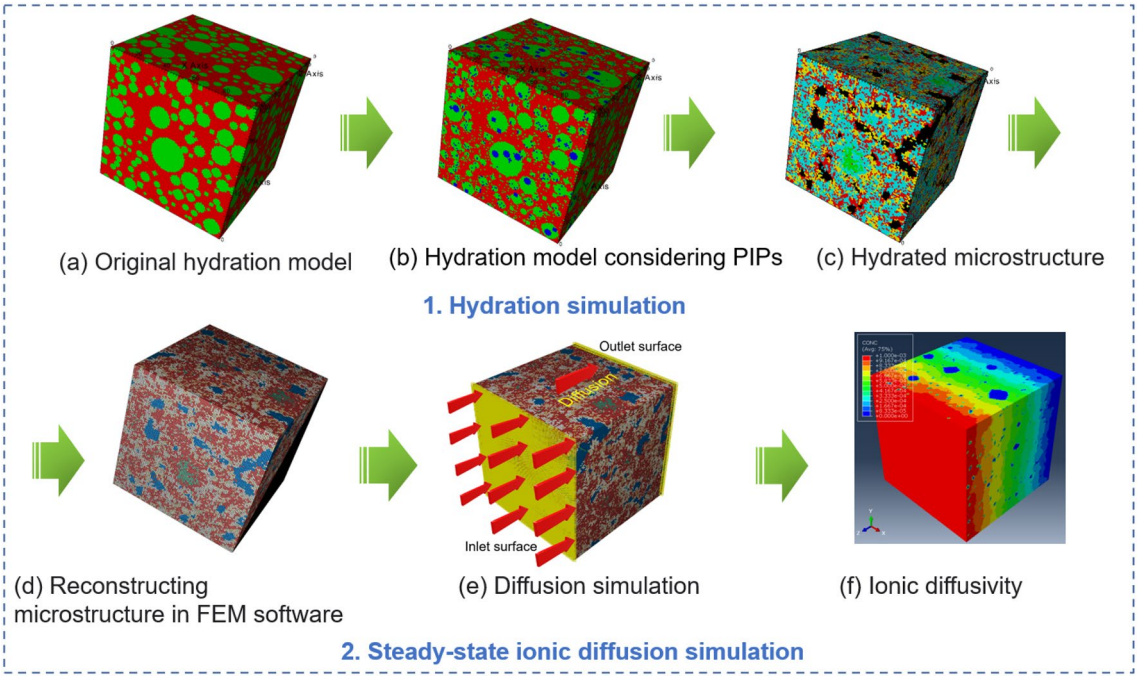

Fig. 1 Simulation method

cement and predict ionic diffusion (Carrara et al., 2016; Patel et al., 2018; Tao, 2020). This method considers various characteristic features of microstructure and allows for a more comprehensive analysis, including the individual contributions of different substances to the overall effective diffusion coefficient of cement paste. However, a critical limitation of existing microstructure-based methods is the common assumption of non-porous cement particles. This simplification neglects the presence and influence of porosity within cement particles (e.g., PIPs), which can significantly impact ionic transport. Indeed, while the importance of overall porosity is well-established, the specific contribution of PIPs to ionic diffusivity has received little attention in current research. Existing models largely overlook the potential for PIPs to act as interconnected pathways for ionic transport, influencing the overall diffusion behavior of cement paste.

Therefore, this study addresses this critical gap by developing a diffusion model that explicitly considers the effects of PIPs. The continuous particle size distribution and PIP size distribution were discretized, and an algorithm for generating PIPs was developed to construct the initial hydration microstructure. The existing hydration model was appropriately upgraded to incorporate effects of PIPs. Moreover, the hydration-diffusion simulations were conducted and the method was validated through the data from experiments. The effective diffusion coefficients obtained with different PIPs were compared, and the effects of w/s ratios and hydration age on the ionic diffusivity of the microstructure considering PIPs were analyzed.

2 Methodology

2.1 The Hydration-Diffusion Method

Figure 1a–f shows the schematic diagram of the hydration-diffusion method. The process of the method consists of several steps, which are as follows:

(1) Microstructure generation with PIPs: First, an algorithm was developed to generate realistic 3D microstructures of unhydrated C_3S particles, explicitly incorporating PIPs with controlled size distributions and porosities. This algorithm allows for precise control PIP size distribution and overall particle porosity.

(2) Hydration simulation: The generated C_3S microstructures were then subjected to a hydration simulation using a modified version of the established CEMHYD3D model. Our modifications made the model be able to consider the influence of PIPs on microstructure development and hydration kinetics. The simulation was performed at a temperature of 25 °C, using a variable time step. The model tracks the evolution of the microstructure, including the

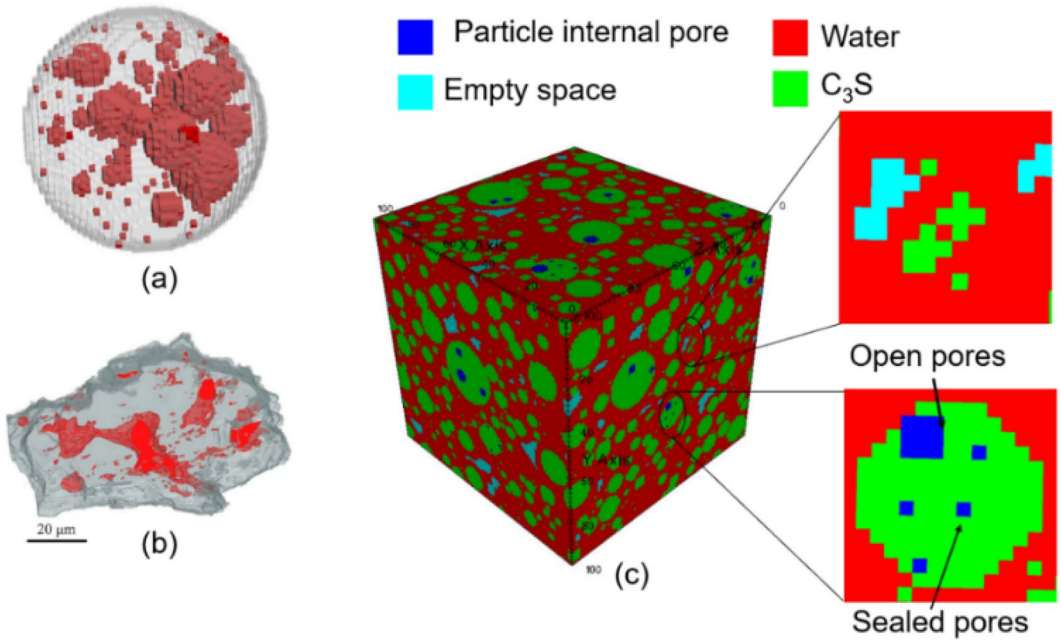

Fig. 2 Initial structures of a C_3S particle and RVE: **a** C_3S particle in the simulation; **b** C_3S particle observed by the SBFSEM system adapted from (Yang et al., 2018); **c** initial structure of RVE considering internal pores

formation of hydration products and the changes in porosity over time.

(3) Finite element reconstruction: The 3D hydrated microstructures were subsequently reconstructed within a finite element method (FEM) software package (ABAQUS), This reconstruction involved importing the voxel-based microstructure data into the FEM software and assigning material properties to each voxel based on its phase composition (C_3S, C-S–H, portlandite, pore solution). The mesh resolution was carefully chosen to represent microstructure, with a characteristic element size of 4.5 μm.

(4) Ionic diffusion simulation: The effects of PIPs on steady-state ionic diffusion were incorporated into the FEM simulation. The boundary conditions were set to a fixed concentration of chloride ions at one boundary and a zero-flux condition at the opposite boundary.

2.2 Construction of İnitial Microstructure with Particle İnternal Pores

2.2.1 Generation of Microstructure with Varying Internal Pore Size Distributions

First, the databases containing the information of microstructure and particles were defined. The microstructure database stored the coordinates of voxels, as well as the corresponding phase labels. On the other hand, the particle database contains particle information of C_3S, including the coordinates of particle center and the associated phase label. The radius of a single C_3S particle was denoted as $r_{0.}$ The generation of PIPs followed a specific algorithm. Initially, a random coordinate in the box with dimensions of $2r_0 \times 2r_0 \times 2r_0$ was selected as the center of the single C_3S particle. Subsequently, the algorithm would check the entire microstructure to determine if there was sufficient space to accommodate pores. The coordinates of PIPs must satisfy Eq. (1).

$$\begin{cases} |x_{IP} - x_0| \le r_0 \\ |y_{IP} - y_0| \le r_0 \\ |z_{IP} - z_0| \le r_0 \\ \sqrt{(x_{IP} - x_0)^2 + (y_{IP} - y_0)^2 + (z_{IP} - z_0)^2} + r_{IP} \le r_0 \end{cases} \tag{1}$$

where x_0, y_0, and z_0 are the coordinates of particle center; x_{IP}, y_{IP}, and z_{IP} are the coordinates of the PIP center; $r_{0.}$ and r_{IP} are the radii of C_3S particle and PIPs, respectively. Figure 2a shows a C_3S particle that incorporates PIPs in the simulation. The single C_3S obtained from the SBFSEM system is shown in Fig. 2b. The RVE for C_3S particles considered sealed pores and open pores is shown in Fig. 2c. In the figure, the dimensions of RVE were set at $100\,\mu m \times 100\,\mu m \times 100\,\mu m$. The dimensions of voxel were set at $1\,\mu m \times 1\,\mu m \times 1\,\mu m$.

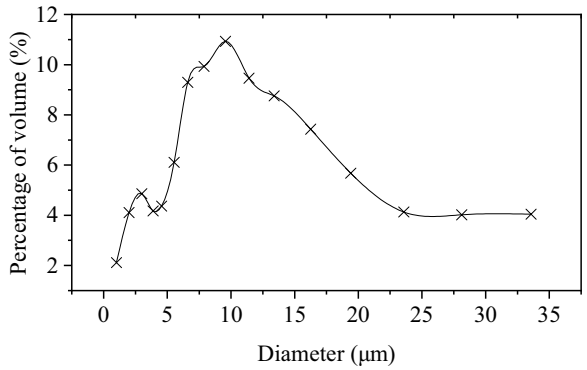

Fig. 3 Particle size distribution of C_3S utilized in the simulation

The particle size distribution employed in the simulation is shown in Fig. 3. The size distribution of PIPs was referred as to the internal pore size distribution (IPSD). In this study, two distinct IPSDs, denoted as IPSD1 and IPSD2, were utilized. In IPSD1, the PIPs were very small and exhibited a narrow pore size distribution. Thus, all PIPs within the microstructure were assumed to have the same size and were represented by individual voxels. Therefore, the volume of a PIP On the other hand, IPSD2 assumed a wider internal pore size distribution than IPSD1.

Figure 4a, b show a typical example of the initial microstructures of C_3S particles for IPSD1 and IPSD2, respectively, obtained at a w/s ratio of 0.4 and a particle porosity (PP) of 4%. Due to the limitation of voxel size, the particle diameter ≤ 1 μm was represented by a single-voxel particle. This approach is consistent with those employed in the literatures (Bentz, 2000, 2005). In IPSD1, each pore was assumed to be a sphere with a volume of 1 μm^3. These idealized small pores were assumed to be randomly distributed within C_3S particles. Figure 5 presents the IPSD2. The results in Fig. 5 indicated that the pores with a radius of 2 μm constitute 43% of the total pore volume, representing the major pore size. In contrast, small pores (radius of 1 μm) account for only 8.8% of the total pore volume. The water content in the RVE was maintained at a constant value for cases with IPSD1 and IPSD2.

2.2.2 *Generation of Microstructure with Different Particle Porosities*

The algorithm for generating the initial microstructure of C_3S particles with different PPs involves three main steps: generation of solid C_3S particles, generation of PIPs and verification of the desired PP value. The detailed procedures were as follows:

Step 1: Solid C_3S particles were randomly placed within the RVE based on the particle information. The particles were arranged in descending order of size, ensuring that they did not overlap with each other.

Step 2: PIPs were generated by removing C_3S voxels from the target particles. First, the algorithm searched database of C_3S particles to locate a target C_3S particle with the specified radius and coordinate. A random location within the target C_3S particle was selected, and the algorithm checked if there was sufficient space to generate a PIP. If the radius of the PIP was smaller than the distance between the PIP center and the target particle surface, the PIP would be created by removing the C_3S voxels within its boundaries. This process continued until the PP value of the target C_3S particle reached the desired value. It was worth noting that as the size of the particles decreases, the accuracy of placing empty voxels within them diminishes, especially when aiming for high PP values. To address this limitation, the accuracy was appropriately reduced for small C_3S particles to meet the modeling requirements.

Step 3: The algorithm checked all the C_3S particles within the RVE and repeated Step 2 until the desired PP value was achieved for all C_3S particles. Figure 6a–d show the initial microstructures of C_3S particles obtained with PP values of 0%, 4%, 6%, and 8%, at w/s ratio of 0.4.

2.3 *Hydration of C_3S Incorporating PIPs and Microstructure Reconstruction*

In this study, the CEMHYD3D model (Bentz, 2000, 2005; Bernard & Kamali-Bernard, 2012; Carrara et al., 2016; Wang et al., 2021) was used to construct the hydrated C_3S microstructures. The original algorithm of CEMHYD3D did not account for the invasion of water into open pores, which limited the reactive surface area of C_3S particles (Bentz, 2000, 2005). To account for the "invading" process of water into open pores, modifications were made to the original CEMHYD3D model. The modified algorithm is described as follows:

Step 1: The modified algorithm checked voxels in the RVE and read the initial chemical and physical parameters.

Step 2: The modified algorithm checked the entire RVE to identify open pores within individual C_3S particles. By scanning the particle database, the algorithm obtained information about the target C_3S particle and searched for it accordingly. The open pores on the particle surface were identified by checking if

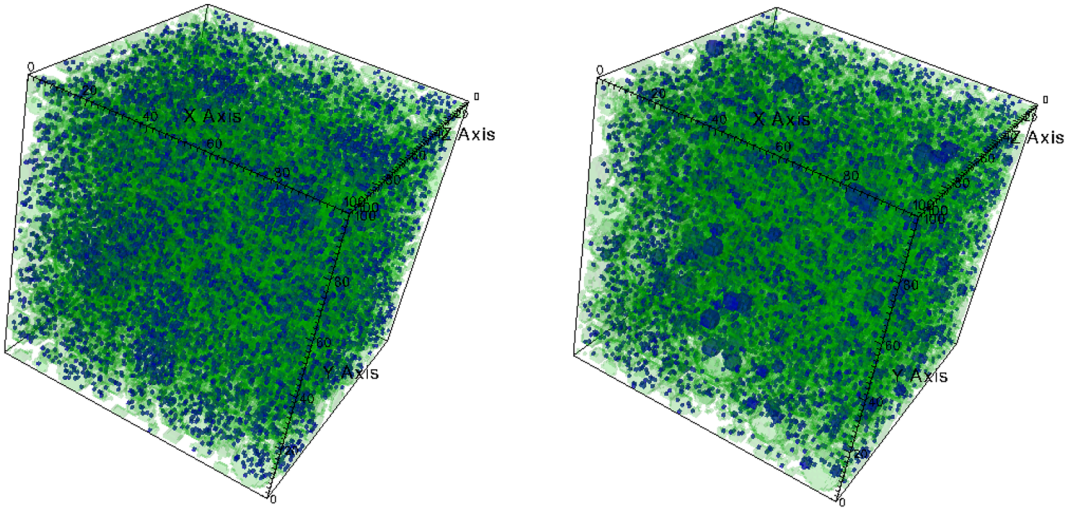

Fig. 4 Microstructure of C_3S particles obtained with different IPSDs at initial w/s = 0.4 and PP = 4%: **a** IPSD1; **b** IPSD2. Green and blue colors represent C_3S and PIPs, respectively

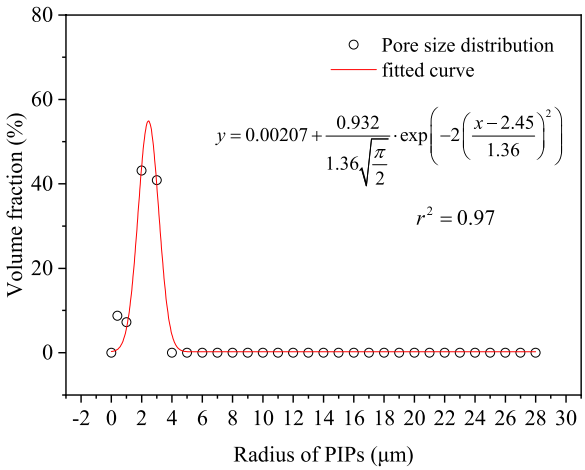

Fig. 5 Pore size distribution for IPSD2

C_3S voxels were in contact with voxels representing aqueous species.

Step 3: The voxels that represent PIPs would change into water voxels if they were in contact with water, and the same number of water voxels would be eliminated from the hydration system.

Step 4: Steps 2 to 3 were repeated until all target particles had been checked.

Step 5: Diffusion and dissolution were performed by the model.

Step 6: Steps 2 to 5 were repeated until the desired simulation cycle was reached for the target particles. Figure 7 shows the evolution of a single C_3S particle during the hydration process when considering PIPs in the modified CEMHYD3D model.

The hydrated microstructure derived from the modified CEMHYD3D model was encapsulated in a numerical sequence denoting distinct phases. This sequential arrangement of numbers was referred to as the string here. For the microstructure characterized by dimensions of $100 \times 100 \times 100$ voxels, this string encompassed a substantial count of 10^6 numerical entities. The subsequent task was to transfer this string from the modified CEMHYD3D model to the FEM software. The detailed procedure is given in (Shen & Wang, 2023). Figure 8a shows the hydrated C_3S microstructure obtained from the modified CEMHYD3D model. The w/s ratio and hydration age were 0.4 and 45 h, respectively. Figure 8b shows the hydrated C_3S microstructure reconstructed within the FEM software.

2.4 Diffusion Simulation

Within the computational framework of ABAQUS software, the DC3D8 element was employed. Figure 9 presents the boundary conditions utilized in the simulation. The ionic concentration at inlet was set to be 1.0 mol · mm^{-3}, whereas at the outlet surface, it was specified to be 0 mol · mm^{-3}.

The flux q_i diffusing through the element i is usually formalized using Eq. (Bernard & Kamali-Bernard, 2010).

$$q_i = -D_i \frac{dc_i}{dx} \tag{2}$$

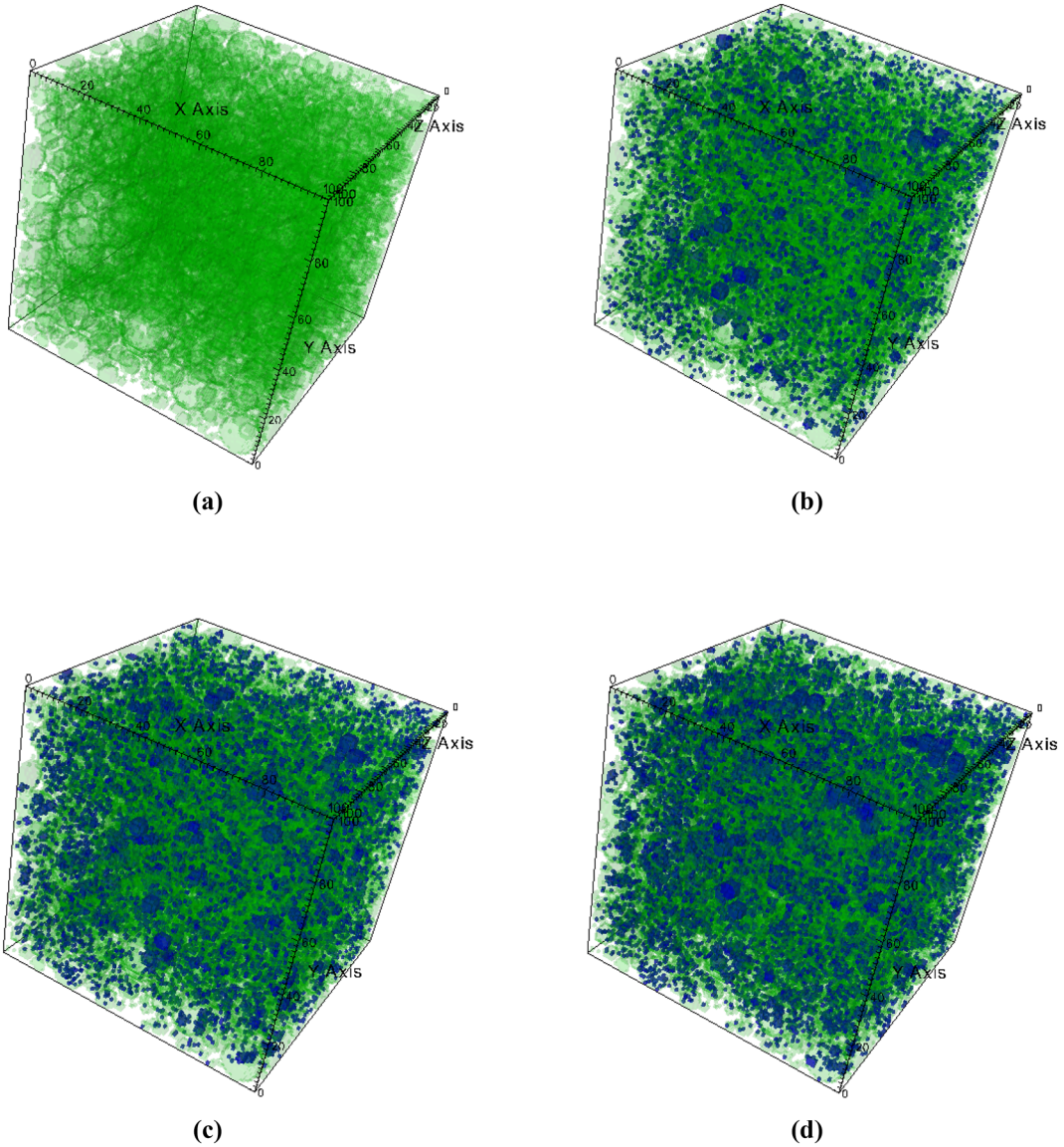

Fig. 6 Initial microstructures obtained with IPSD2 at w/s = 0.4: (**a**) PP = 0%, (**b**) PP = 4%; (**c**) PP = 6%; (**d**) PP = 8%. Green and blue colors represent C_3S and PIPs, respectively

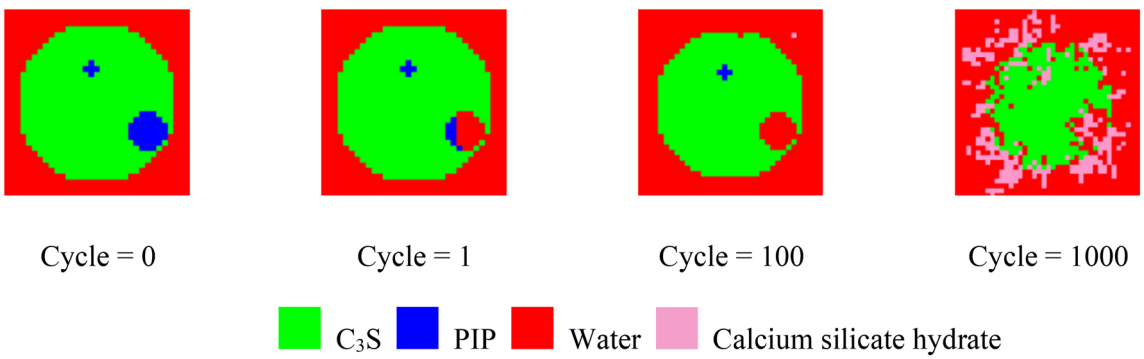

Fig. 7 Evolution of a single C_3S particle obtained from the modified CEMHYD3D model when considering PIPs

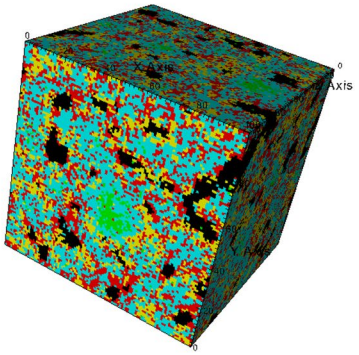

(a) Hydrated C_3S generated from the modified CEMHYD3D model.

(b) C_3S microstructure reconstructed in FEM software.

Fig. 8 Microstructure reconstruction

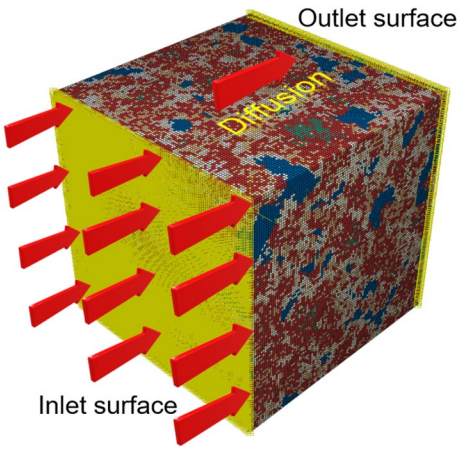

Fig. 9 Boundary conditions utilized in the simulation

where q_i is the flux diffusing through the element i, in $\text{mol} \cdot \text{m}^{-3} \cdot \text{s}^{-1}$; D_i is the diffusion coefficient for element i, in $\text{m}^2 \cdot \text{s}^{-1}$; and dc_i/dx is the gradient of concentration, in $\text{mol} \cdot \text{m}^{-4}$.

The effective diffusion coefficient, D_{eff}, of entire cubic RVE is dependent on multiple critical factors. These factors encompass the magnitude of the diffusive flux, the effective surface area participating in diffusion, the length of the diffusion pathway, and the concentration gradient established between the inlet and outlet boundaries. The quantification of this coefficient can be achieved through the utilization of Eq. (3) (L. Liu et al., 2020a, 2020b; Zhang, 2013).

$$D_{\text{eff}} = \frac{Q}{A} \cdot \frac{L_s}{C_{\text{in}} - C_{\text{out}}} \tag{3}$$

where D_{eff} is effective diffusion coefficient, in $\text{m}^2 \cdot \text{s}^{-1}$; Q represents the flux traversing the designated outlet surface, in $\text{mol} \cdot \text{m}^{-2} \cdot \text{s}^{-1}$; L_s denotes specimen thickness, in m; C_{in} and C_{out} are the concentration of diffusing substance at inlet and outlet surfaces, respectively, in $\text{mol} \cdot \text{m}^{-3}$.

In the simulation, a unit system was established within the ABAQUS software. It was postulated that within ABAQUS, the side length of RVE corresponded to one λ. 1λ was equivalent to 100 μm. Consequently, the total flux, denoted as Q_i, passing through the element with the diffusing surface of $10^{-4}\lambda^2$ could be represented utilizing Eq. (4).

$$Q_i = q_i \cdot \frac{\text{mol}}{\lambda^2 \cdot \text{s}} \cdot \overbrace{10^{-4}\lambda^2}^{\textit{area of an element}} = q_i \cdot \frac{\text{mol}}{\text{s}} 10^{-4} \tag{4}$$

Then, the flux, Q, passing through the entire surface of RVE was deduced as expressed in Eq. (5).

$$Q = Q_1 + Q_2 + \cdots + Q_n = \left(\sum_{i=1}^{n} q_i \right) \frac{\text{mol}}{\text{s}} \cdot 10^{-4} \tag{5}$$

The determination of the D_{eff} for hydrated C_3S was facilitated through the integration of Eq. (5) into Eq. (3), leading to a refined formulation denoted in Eq. (6).

$$D_{\text{eff}} = \frac{\left(\sum_{i=1}^{n} q_i \right) \frac{\text{mol}}{\text{s}} \cdot 10^{-4}}{\lambda^2} \cdot \frac{\lambda}{10^{-3} \frac{\text{mol}}{\text{s} \cdot \lambda^3}} = \left(\sum_{i=1}^{n} q_i \right) \cdot 10^{-9} \cdot \text{m}^2 \cdot \text{s}^{-1} \tag{6}$$

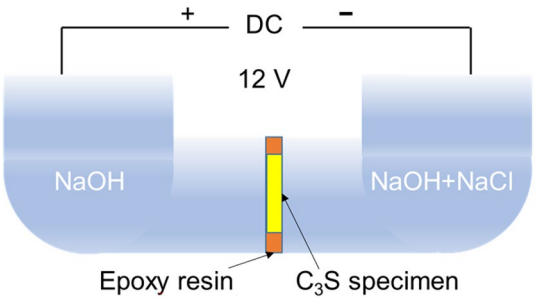

Fig. 10 Schematic diagram of electro-migration experimental setup

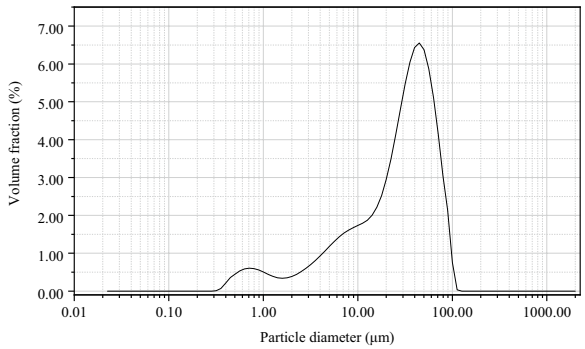

Fig. 11 Particle size distribution of C_3S

3 Comparison of Experimental Results and Simulated Results

The simulated effective diffusion coefficients for chloride ions in hydrated C_3S paste were compared with experimental results derived from electro-migration experiments. The experimental setup is depicted in Fig. 10. The volumes for the anode and cathode compartments were both 100 mL. The concentrations of NaOH and NaCl in the compartments were 0.3 mol · L^{-1} and 1 mol · L^{-1}, respectively. The C_3S was synthesized via solid-state reaction using high-purity quartz powder and calcium carbonate ($CaCO_3$) as precursors. The reactants were combined in a stoichiometric ratio of 1:3 (SiO_2:$CaCO_3$) and subsequently subjected to thermal treatment in an electric furnace. The mixture was heated to 1650 °C and maintained at this temperature for 10 h to facilitate the formation of C_3S. Following the heating period, the resulting material was rapidly quenched on a platinum dish, employing a firing cycle consistent with the procedure detailed in (Costoya Fernández, 2008). The synthesized C_3S clinker was then comminuted via grinding and sieved to obtain a homogenous powder. Finally, the particle size distribution of the C_3S employed in experiment was obtained using a Malvern Mastersizer 2000 laser-diffraction analyzer, as shown in Fig. 11. Disk-shaped C_3S specimens used in the electro-migration experiment were prepared using a rubber mold with a diameter of 42 mm and a thickness of 4 mm.

The calculation of the effective chloride diffusion coefficient was performed using Eq. (7) (Andrade, 1993; Tao, 2020).

$$D_{\text{eff}} = \frac{RTLV_{\text{an}}}{ZF\Delta EC_s A} \cdot \frac{\Delta C_1}{\Delta t} \tag{7}$$

where R is the gas constant, in J · K^{-1} · mol^{-1}; L represents specimen thickness, in m; V_{an} is the capacity of compartment connected to anode, in m^3; Δt is the time, in s; T is absolute temperature, in K; Z is the electric charge; F is the Faraday's number; C_s is the concentration in cathode compartment, in mol · L^{-1}. A is the area of diffusion surface, in m^2; and ΔC_1 is the concentration difference, in mol · L^{-1}.

In this section, the RVE dimensions were determined through a convergence study, iteratively increasing the volume until the random sequential addition method could accommodate all particles. The dimension of voxel was assumed to be 1/100 of the size of RVE. Therefore, the dimensions of RVE were set at 450μm ×450μm×450μm, with voxel dimensions of 4.5μm ×4.5μm×4.5μm. The simulation scenario for the C_3S paste incorporating PIPs was denoted as Case A here. The values of D_{eff} were calculated for hydrated C_3S paste with PPs of 0%, 4%, 6%, 8%, and 10%. The values of D_{eff} for solid phases were assumed to be 0 $m^2 \cdot s^{-1}$. The values of D_{eff} for water was adopted from the reference (L. Liu et al., 2020a, 2020b). The D_{eff} for C-S–H was determined through iterative adjustments based on literature values [see reference (Dridi, 2013)] until the simulation results closely matched the experimental data. The values of D_{eff} for C-S–H and water in the RVE were set as 0.93×10^{-12} and 2.03×10^{-9} $m^2 \cdot s^{-1}$, respectively. The particle size distribution employed in the simulation was the same as that utilized in the experiment. In the experiment, the chloride diffusion can be affected by the properties of pore solution, as suggested by previous studies (Tang, 1999a, 1999b; Zhang et al., 2021). The approach used for considering the effects of pore solution is given elsewhere (Zhang et al., 2021). The experimental results from literatures can be found in (Ngala et al., 1995; Poupard et al., 2004; Tao, 2020; Wilson et al., 2021). The specific parameters utilized in the simulation are summarized in Table 1

The simulation method proposed in this study was also compared with method reported in the reference (Wang et al., 2025), which accounts for the effects of pore solution properties. The particle size distribution utilized in the simulation was identical to that shown in Fig. 11. The key parameters and calculated results

Table 1 Simulation parameters for the proposed method

Parameter	Symbol	Value	Units
RVE size	L_{RVE}	450	μm
Voxel size	L_{Voxel}	4.5	μm
Particle porosity	PP	4	%
Particle porosity	PP	6	%
Particle porosity	PP	8	%
Particle porosity	PP	10	%
Effective diffusion coefficient for water	$D_{\text{eff\_water}}$	2.03×10^{-9}	$m^2\cdot s^{-1}$
Effective diffusion coefficient for C-S–H	$D_{\text{eff\_C-S-H}}$	0.93×10^{-12}	$m^2\cdot s^{-1}$
Effective diffusion coefficient for solid phases	$D_{\text{eff\_solid}}$	0	$m^2\cdot s^{-1}$
Ionic concentration at inlet surface	C_{inlet}	1	$mol\cdot mm^{-3}$
Ionic concentration at outlet surface	C_{outlet}	0	$mol\cdot mm^{-3}$

Table 2 Key parameters utilized in method from reference (Wang et al., 2025)

Parameter	Symbol	Value	Units
RVE size	L_{RVE}	450	μm
Voxel size	L_{Voxel}	4.5	μm
Effective diffusion coefficient for water	$D_{\text{eff\_water}}$	2.03×10^{-9}	$m^2\cdot s^{-1}$
Effective diffusion coefficient for C-S–H at w/s = 0.3	$D_{\text{C-S-H\_0.3}}$	0.890×10^{-12}	$m^2\cdot s^{-1}$
Effective diffusion coefficient for C-S–H at w/s = 0.4	$D_{\text{C-S-H\_0.4}}$	0.933×10^{-12}	$m^2\cdot s^{-1}$
Effective diffusion coefficient for C-S–H at w/s = 0.5	$D_{\text{C-S-H\_0.5}}$	0.996×10^{-12}	$m^2\cdot s^{-1}$
Effective diffusion coefficient for solid phases	$D_{\text{eff\_solid}}$	0	$m^2\cdot s^{-1}$
Ionic concentration at inlet surface	C_{inlet}	1	$mol\cdot mm^{-3}$
Ionic concentration at outlet surface	C_{outlet}	0	$mol\cdot mm^{-3}$
Parameter related to chemical activity	B^*	0.045	$dm\cdot mol^{-1}$
Dimensionless parameter governed by ion mobility	$K_{\tau 0}$	− 0.207	–
Drift velocity induced by the semi-membrane effect	$K_{\tau m}$	− 0.402	–

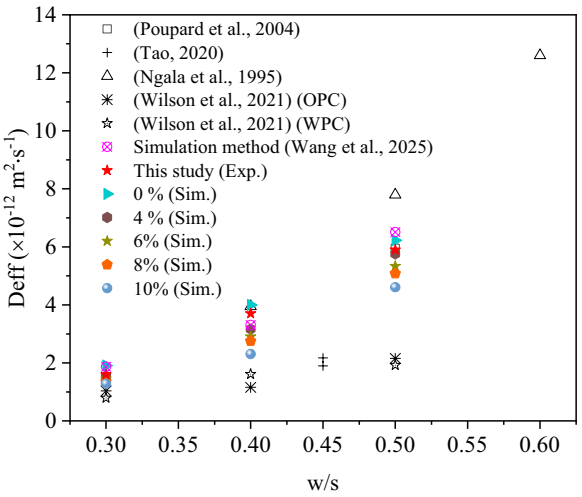

Fig. 12 Experimental and simulated effective diffusion coefficients

are presented in Table 2 and Fig. 12, respectively. The results obtained using the method in (Wang et al., 2025) were slightly higher than those obtained considering PIPs, however, both methods generally agreed with experimental results.

The simulated and experimental results are presented in Fig. 12, indicating the D_{eff} for C_3S paste samples with varying PP and w/s ratios. For C_3S paste with a PP of 0% at w/s ratios of 0.3, 0.4, and 0.5, the calculated chloride effective diffusion coefficients were found to be 1.91×10^{-12}, 4.00×10^{-12}, 6.23×10^{-12} $m^2\cdot s^{-1}$, respectively. These results exhibited an increasing trend with higher w/s ratios, indicating that C_3S paste with a higher w/s ratio would offer more pathways for chloride diffusion compared with a lower w/s ratio. Furthermore, for C_3S paste at a w/s ratio of 0.3 with varying PP values of 0%, 4%, 6%, 8%, and 10%, the corresponding chloride

effective diffusion coefficients were determined as 1.91×10^{-12}, 1.54×10^{-12}, 1.45×10^{-12}, 1.35×10^{-12}, and 1.28×10^{-12} $m^2{\cdot}s^{-1}$, respectively. These values decreased as the PP increased. Similar trends were also observed for cases with w/s ratios of 0.4 and 0.5. This phenomenon can be attributed to the faster hydration process of C_3S particles with higher PP, resulting in a reduced presence of capillary pores (CPs) and fewer pathways for chloride diffusion. The effect is particularly evident at the early ages of hydration. However, at later ages, the PP showed less influence on the value of D_{eff}.

4 Results and Discussion

Three cases were simulated to examine the effects of PIPs on ionic diffusion in hydrated C_3S paste. In the first case (Case I), PIPs were generated by removing C_3S voxels from the RVEs. In the second case (Case II), the C_3S content in initial microstructures remained the same. To ensure this, additional C_3S particles were added to the RVEs. The third case (Case III) assumed that the w/s ratio of the C_3S paste within initial microstructures remained constant. To achieve this, extra C_3S particles were added to RVEs to adjust the w/s ratio accordingly. A schematic diagram illustrating these three cases is presented in Fig. 13. The values of D_{eff} obtained from different cases with IPSD1 are shown in Table 3.

4.1 Effect of Size Distribution of Particle Internal Pores

Figure 14a, b show D_{eff} obtained from Case I with different IPSDs. The size distribution of PIPs had a significant impact on the D_{eff}, as shown in Fig. 14. The values for D_{eff} obtained from the simulation with a wide size distribution of PIP were larger than those obtained with a narrow pore size distribution. This is evident in Fig. 14a, where D_{eff} increased by 4.5×10^{-13}, 8.3×10^{-13}, 7.5×10^{-13}, and 13.2×10^{-13} $m^2{\cdot}s^{-1}$ for IPSD2 at 4%, 6%, 8%, and 10%, respectively, compared with those obtained from IPSD1. Similar results can be observed in Fig. 14b, c. These results indicated that a wider PIP size distribution would lead to a higher ionic diffusivity than a narrower one when the water content in the RVEs was fixed.

The difference between the D_{eff} obtained from IPSD1 and IPSD2, represented by ΔD_{eff}, is shown in Fig. 15. In the Figure, the values of D_{eff} at 3, 7, 28, and 56 days obtained with PP of 4% and w/s ratio of 0.4 were 0.45×10^{-13}, 0.38×10^{-13}, 0.15×10^{-13}, and 0.05×10^{-13} $m^2{\cdot}s^{-1}$, respectively. The value decreased with the increase of hydration age. Similar results were observed for simulations with PP of 6%, 8%, and 10%. These results indicated that the difference between the D_{eff} with a wide size distribution of PIP and that with a narrow size distribution of PIP would decrease as hydration age increased. This phenomenon could be attributed to the differences in the hydration rate induced by the variation in size distributions of PIP.

Figure 16 shows the hydration rate obtained from Case I with IPSD1 and IPSD2 at w/s = 0.4. The PP utilized in the simulation was about 8%. The hydration rate was determined as the first derivative of the degree of hydration. As shown in Fig. 16, at 7.2 h, the hydration rate for IPSD1 and IPSD2 was calculated as 0.02217 and 0.01826 h^{-1}, respectively. It was observed that the hydration rate obtained with IPSD1 was higher than that obtained with IPSD2 at early ages of hydration. Thus, the microstructure development of C_3S paste obtained with IPSD1 was expected to exhibit faster progress compared with that achieved with IPSD2 during the early ages of hydration.

Figure 17a shows the evolution of D_{eff} obtained from Case II, comparing IPSD1 and IPSD2 at w/s = 0.4, with varying PP values. The average difference between D_{eff} values obtained from IPSD1 and IPSD2 at 3 days was only 2.1×10^{-13} $m^2{\cdot}s^{-1}$. Initially, the D_{eff} obtained from IPSD2 was larger than that obtained from IPSD1, which could be attributed to the higher hydration rate for IPSD1 during the early ages of hydration. However, as the hydration age progressed to 7, 28, and 56 days, the curves representing D_{eff} obtained from IPSD1 and IPSD2 exhibited significant overlap. In Case II, the standard deviation for ΔD_{eff} at 3, 7, 28, and 56 days was determined as 12.5×10^{-5}, 6.16×10^{-5}, 7.80×10^{-5}, and 6.83×10^{-5}, respectively. Similar results were also made in Case III, as presented in Fig. 17b. These results demonstrated that at later ages of hydration, the difference in ionic diffusivity induced by the size distribution of PIP did not exhibit a significant change. This could be attributed to the similar degree of hydration and microstructure achieved between IPSD1 and IPSD2 at later ages.

4.2 Effect of Particle Porosity

Figure 18 shows the evolution of D_{eff} obtained from Case I considering different values of PP. The simulation employed a w/s ratio of 0.4 and PIPs with a pore size distribution of IPSD1. In Fig. 18, at 3 days, D_{eff} exhibited an increase of 2.0%, 2.1%, 3.4%, and 5.8% for PP of 4%, 6%, 8%, and 10%, respectively, compared with PP of 0%. This trend of increasing D_{eff} was consistently observed at 7, 28, and 56 days. These results indicated that, while maintaining a constant water content for different hydration systems, an increase in PP would lead to an increase in D_{eff}. This phenomenon was attributed to the decrease in the content of C_3S within the system. For a system with a fixed water content, the rise in PP would increase hydration rate and contribute to microstructure development. Although the microstructure development

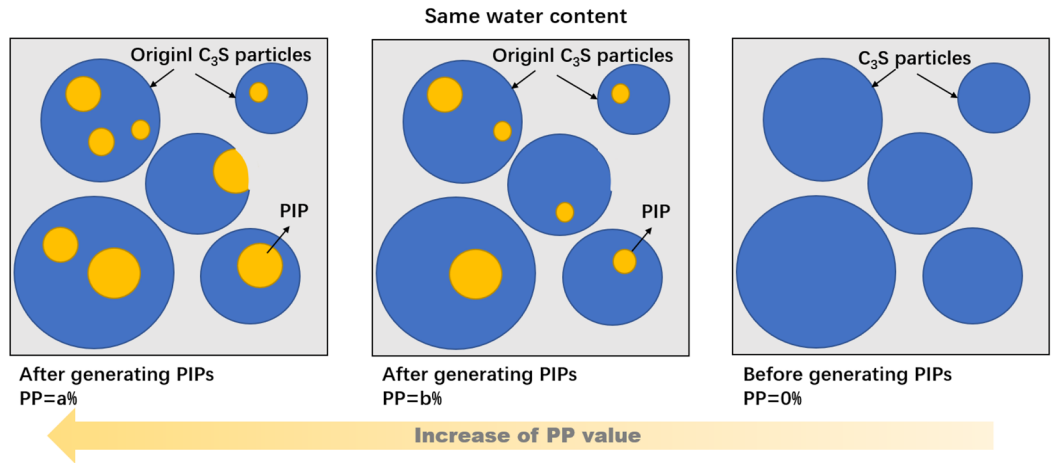

(a)

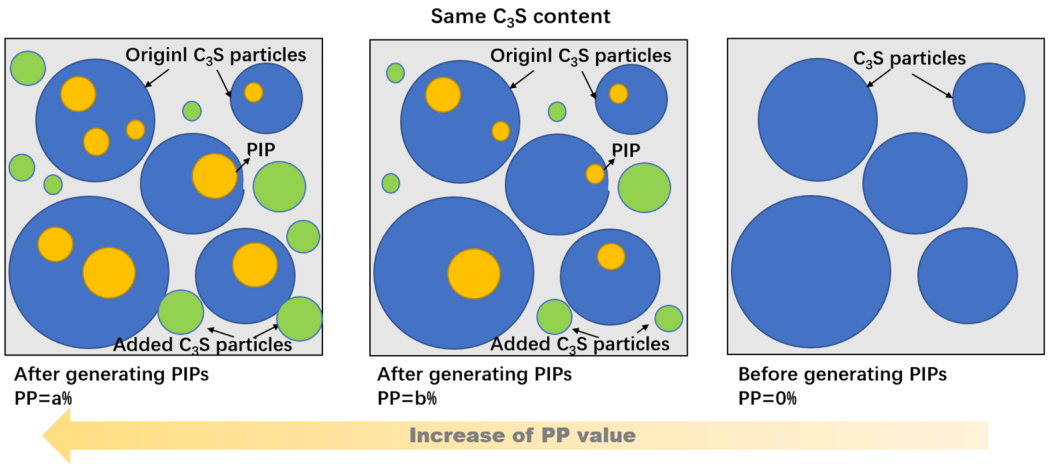

(b)

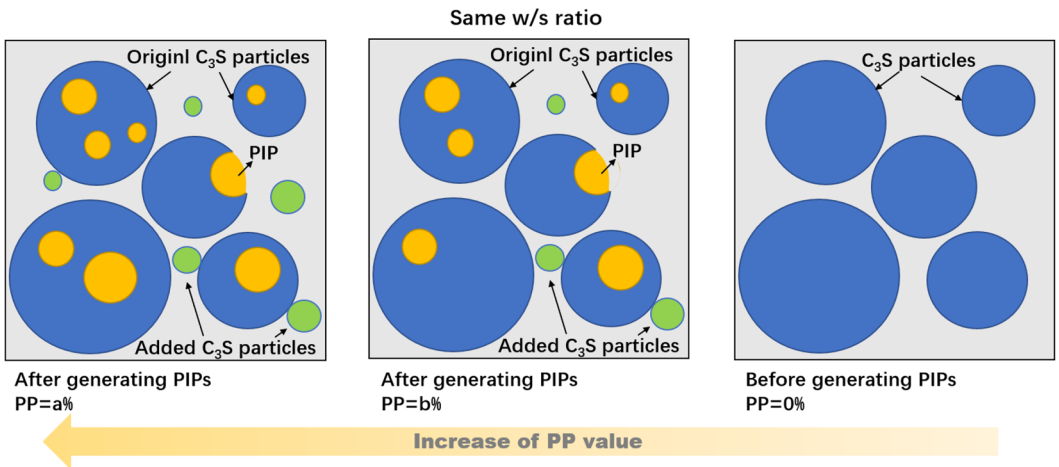

(c)

Fig. 13 Schematic diagram of cases for C_3S microstructures considering PIPs: (**a**) Case I; (**b**) Case II; (**c**) Case III

Table 3 D_{eff} of hydrated C_3S obtained from different cases with IPSD1

Case	Hydration age (days)	Initial w/s ratio	D_{eff} ($\times 10^{-9}$ $m^2 \cdot s^{-1}$)				
			PP = 0%	PP = 4%	PP = 6%	PP = 8%	PP = 10%
I	3	0.4	0.01679	0.01717	0.01715	0.01736	0.01778
		0.5	0.0244	0.02428	0.02453	0.02464	0.02499
		0.6	0.03185	0.03191	0.0319	0.03167	0.03218
	7	0.4	0.01027	0.01115	0.01156	0.01186	0.01253
		0.5	0.01683	0.01755	0.01811	0.01866	0.01942
		0.6	0.02401	0.02493	0.02543	0.02572	0.02673
	28	0.4	0.00623	0.00677	0.00715	0.00742	0.00791
		0.5	0.01058	0.0118	0.01274	0.01351	0.01463
		0.6	0.01727	0.01921	0.02009	0.02085	0.02216
	56	0.4	0.00569	0.00624	0.00654	0.0068	0.00717
		0.5	0.00941	0.0107	0.01171	0.01254	0.0137
		0.6	0.01616	0.01828	0.01914	0.02002	0.02144
II	3	0.4	0.01679	0.0144	0.01347	0.01266	0.01208
		0.5	0.0244	0.0216	0.02042	0.01948	0.01854
		0.6	0.03185	0.0289	0.0275	0.02632	0.0254
	7	0.4	0.01027	0.00912	0.00884	0.00824	0.00806
		0.5	0.01683	0.01537	0.01471	0.0142	0.01377
		0.6	0.02401	0.02231	0.02154	0.0208	0.02037
	28	0.4	0.00623	0.00596	0.00603	0.0058	0.00577
		0.5	0.01058	0.00995	0.0097	0.00942	0.00934
		0.6	0.01727	0.01664	0.01632	0.016	0.01593
	56	0.4	0.00569	0.00556	0.00562	0.00541	0.00542
		0.5	0.00941	0.00891	0.0087	0.00845	0.00838
		0.6	0.01616	0.01564	0.01541	0.01512	0.01509
III	3	0.4	0.01679	0.01581	0.01527	0.01493	0.01475
		0.5	0.0244	0.02283	0.02214	0.02177	0.02098
		0.6	0.03185	0.02968	0.02891	0.02825	0.0275
	7	0.4	0.0103	0.01022	0.01007	0.01001	0.01014
		0.5	0.01683	0.01637	0.01611	0.01619	0.01581
		0.6	0.02401	0.02306	0.02272	0.0226	0.02232
	28	0.4	0.00623	0.00644	0.00635	0.00654	0.00664
		0.5	0.01058	0.01083	0.01084	0.01121	0.01113
		0.6	0.01727	0.01746	0.01754	0.01778	0.01787
	56	0.4	0.00569	0.00595	0.00587	0.00606	0.00618
		0.5	0.00941	0.00975	0.0098	0.01017	0.01016
		0.6	0.01616	0.01641	0.0166	0.01688	0.01706

would limit the available pathway for ionic diffusion, the D_{eff} value still increased as PP increased (see Fig. 18). Therefore, the influence of PP on D_{eff} was more significant than the constraining effect on ionic diffusion caused by microstructure development.

Figure 19a, b show the evolution of different phases in Case I with PPs of 0% and 10%, respectively, at a w/s ratio of 0.4. In the simulation, the empty and porosity voxels in CEMHYD3D were defined as the CP voxels here. Figure 19c shows the number of CP voxels obtained for PPs of 0% and 10% during the hydration process in the RVE with a fixed water content. In Fig. 19c, for both simulations, the content of CPs decreased as the hydration age progressed. It was evident that the value for the PP of 10% was larger than that for the PP of 0% throughout the entire hydration process (0–56 h), as shown in Fig. 19c. It is widely accepted that there is a positive correlation between microstructure porosity and ionic diffusivity. Therefore, the results regarding CP voxels support the conclusion that a higher PP would lead

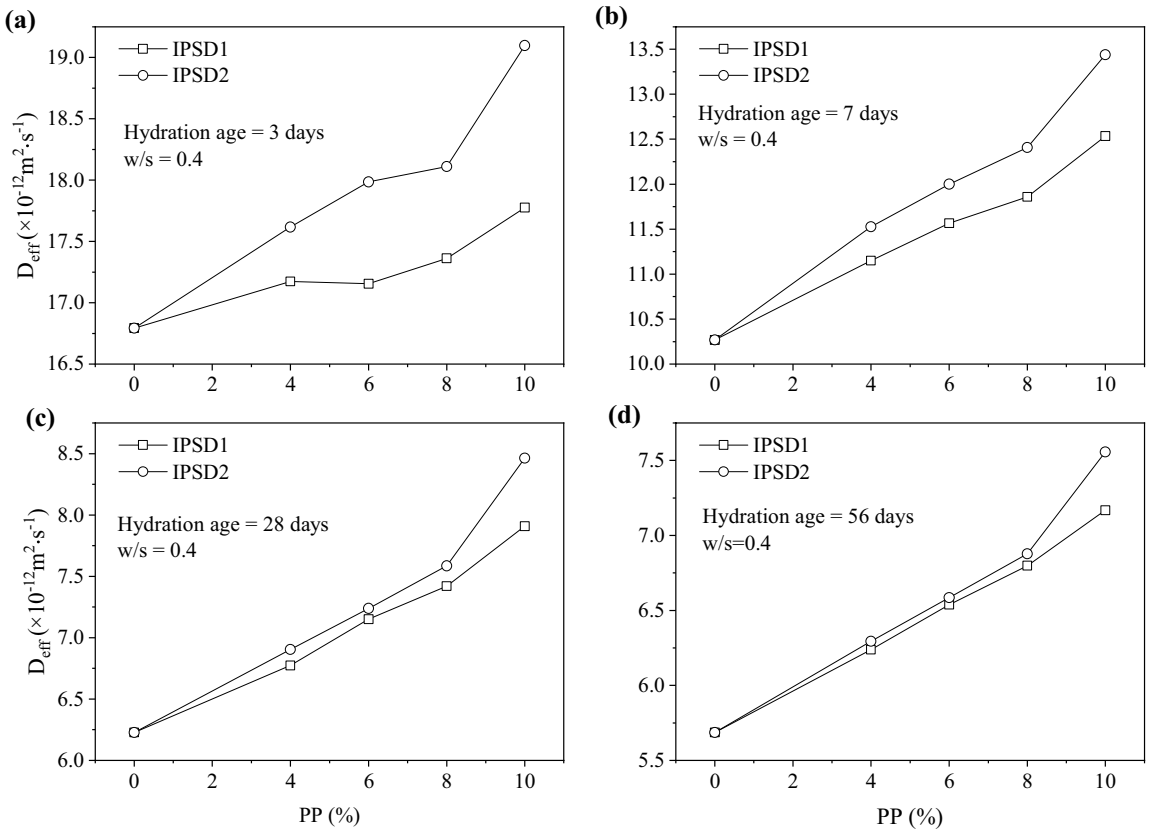

Fig. 14 Effective diffusion coefficients obtained from Case I with different IPSDs at w/s = 0.4. (**a**) Hydration age = 3 days; (**b**) Hydration age = 7 days; Hydration age = 28

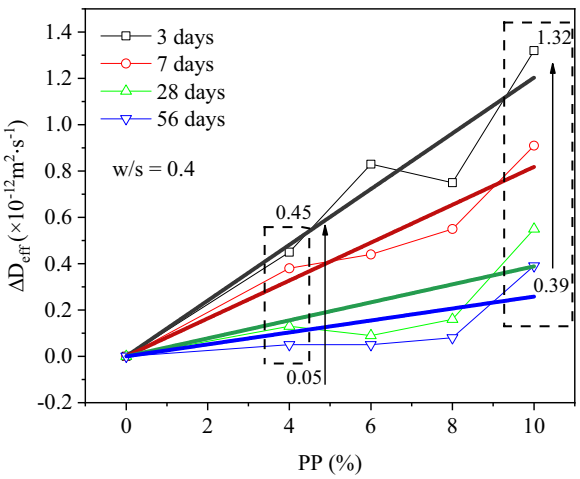

Fig. 15 Differences between effective diffusion coefficients obtained with IPSD1 and IPSD2

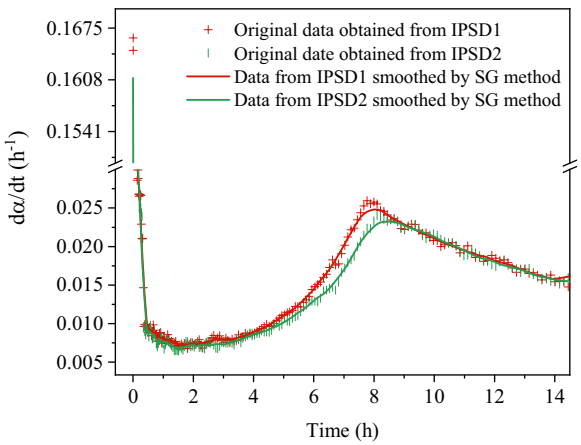

Fig. 16 Hydration rate obtained from Case I with different IPSDs at w/s = 0.4. SG represents Savitzky–Golay filter

to a higher D_{eff} when the water content was maintained at the same level for different RVEs.

Figure 20 shows the D_{eff} curves obtained from Case II using PPs of 0%, 2%, 4%, 6%, 8%, and 10%. The simulation employed a w/s ratio of 0.4 and PIPs with an internal pore size distribution of IPSD1. At early ages of hydration, the D_{eff} obtained from Case II exhibited a decrease with increasing PP. This trend is evidently observed in Fig. 20, where the D_{eff} obtained with a PP

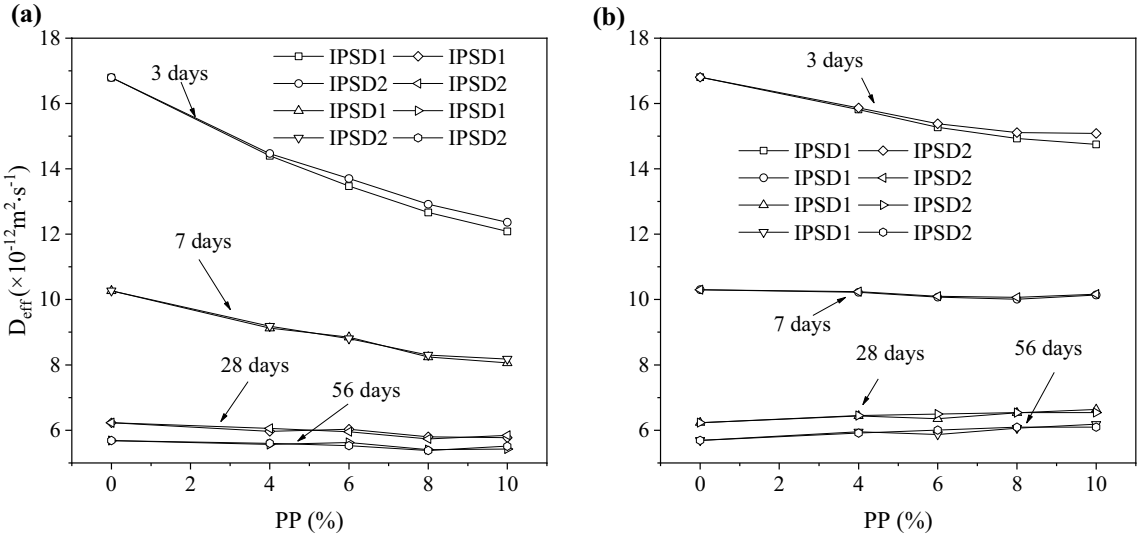

Fig. 17 Comparison of D_{eff} obtained from different cases: (**a**) Case II; (**b**) Case III

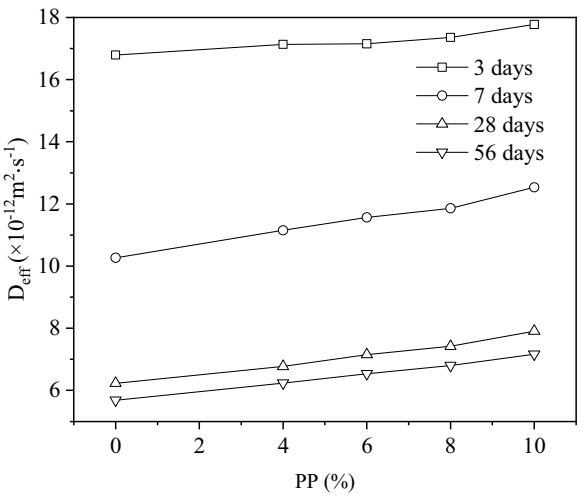

Fig. 18 D_{eff} obtained from Case I with different PPs at w/s = 0.4

of 10% at 3 days decreased by 28% compared with that obtained with a PP of 0% at the same hydration age. Similar results were observed at hydration ages of 7, 28, and 58 days. These findings indicated that a higher PP would lead to a lower ionic diffusivity compared with a lower PP, considering a fixed C_3S content. In Fig. 20, it can be observed that at 56 days, the D_{eff} obtained with a PP of 10% only decreased by 5.1% compared with that with a PP of 0%. The results indicated that the effect of PP on ionic diffusivity weakened as the hydration age increased.

Figure 21a, b show the evolution of phase contents and number of CP voxels obtained from Case II. The number of CP voxels obtained with PP of 10% was compared with that obtained with PP of 0%, as shown in Fig. 21b. At 3 days of hydration, the number of CP voxels for PP = 0% and PP = 10% were 302608 and 264315, respectively. Therefore, at early ages of hydration (before 14.9 days), the number of CP voxels obtained with PP of 0% was higher than that obtained with PP of 10%. This may be ascribed to that the hydration system with a higher PP would hydrate faster than that with a lower PP. However, at 50 days of hydration, the number of CP voxels for PP of 0% and that of 10% was 175503 and 182884, respectively. The results indicated that at late ages of hydration (after 14.9 days), the number of CP voxels obtained with PP of 10% would be little bit higher than that obtained with PP of 0%. Because at later ages of hydration, the degree of hydration for the system with different PPs were very high, and the hydrated microstructures rarely changed as the hydration age progressed. Under this circumstance, some sealed pores within C_3S particles turned into open pores, which increased the number of CP voxels.

Figure 22 shows the D_{eff} obtained from Case III with the PP of 0%, 2%, 4%, 6%, 8%, and 10%. The w/s ratio and PIP size distribution utilized in the simulation remained consistent with those employed in the preceding section. In Fig. 22, the D_{eff} decreased with the increase of PP at 3 days, indicating that a higher PP would lead to a low ionic diffusivity at early ages of hydration when w/s ratios were fixed. However, for the hydration age of the 28 and 56 days, the D_{eff} would slightly increase with the increase of PP. The results were ascribed to the differences in C_3S content and the evolution of PIPs. The number of C_3S voxels in the RVE for PP of 0%, 2%, 4%, 6%, 8%, and 10%

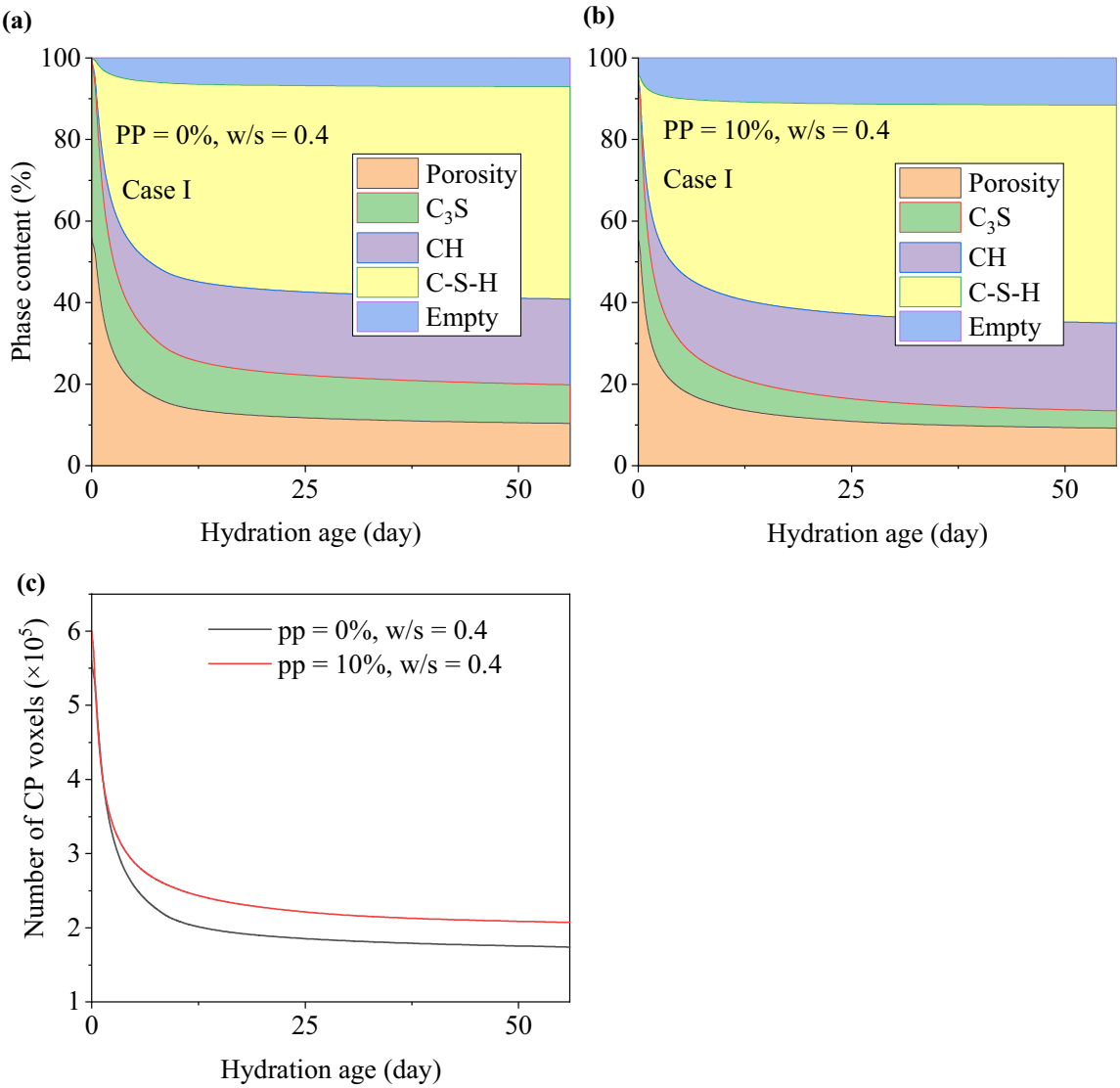

Fig. 19 Evolution of phase contents and number of CP voxels in Case I with PPs of 0% and 10%: (**a**) PP = 0%; (**b**) PP = 10%; (**c**) Number of CP voxels

at w/s = 0.4 was 439798, 430225, 426873, 423528, and 419151, respectively. Therefore, when the w/s ratio was fixed, the C_3S content would slightly decrease with the increase of PP. The decrease of C_3S content would further increase CP voxels, and therefore rise in D_{eff}. However, the increase of PP would also increase hydration rate, decreasing the number of CP voxels at early ages of hydration. Thus, it is not certain how does CP voxels change during the hydration process. To address this issue, the CP voxels obtained from hydration model were used to analyze the process, as shown in Fig. 23.

Figure 23a shows the evolution of phase contents obtained from Case III with a PP of 10%. At 3 days, the number of CP voxels for PP = 0% and PP = 10% were 302608 and 291698, respectively, as shown in Fig. 23b.

Notably, prior to 4.5 days, the number of CP voxels obtained with a PP of 0% exceeded those obtained with a PP of 10%. This observation indicated that the system with a higher PP would contribute to microstructural development and would decrease ionic diffusivity during the early ages of hydration when compared with the one with lower PP. At 50 days, the number of CP voxels for PP = 0% and PP = 10% was 175485 and 192333, respectively. The number of CP voxels obtained with a PP of 0% was lower than that obtained with a PP of 10%, which was attributed to the slow progression of hydration and the change from sealed PIPs to open PIPs. Moreover, in

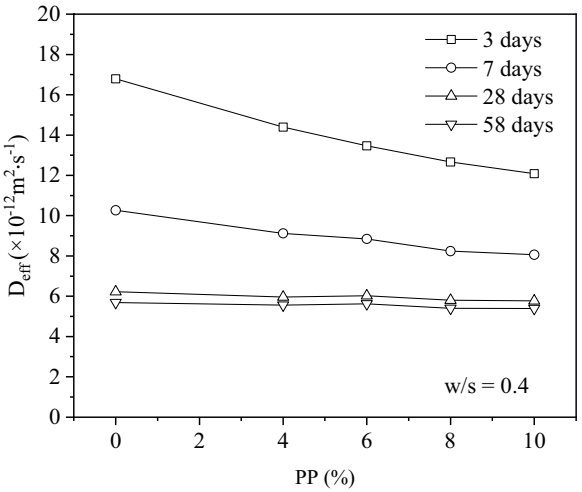

Fig. 20 D_{eff} obtained from Case II with different PPs at w/s = 0.4

Case III, the content of C_3S with PP of 10% was less than that with PP of 0%, further contributing to the increased number of CP voxels in the system. Therefore, the D_{eff} would slightly increase as PP increased during the later ages of hydration.

4.3 Effect of Hydration Age

In this section, a quantitative analysis was conducted to investigate the effects of hydration age on effective diffusion coefficient. The simulation utilized the same w/s ratio and IPSD as in the previous sections. Figure 24a–d show the evolution of D_{eff} obtained from Cases I, II, and III. In Fig. 24, it is evident that regardless of PP, the D_{eff} obtained from all three cases exhibited a decreasing trend as the hydration age increased.

In Case I, the D_{eff} at 3 days decreased from 17.8×10^{-12} to 16.8×10^{-12} $m^2 \cdot s^{-1}$, and at 56 days it further decreased from 7.2×10^{-12} to 5.7×10^{-12} $m^2 \cdot s^{-1}$. The difference between the maximum and minimum D_{eff} values at 3 and 56 days was 1.0 and 1.5 $m^2 \cdot s^{-1}$, respectively. The difference value for D_{eff} at 56 days increased by 50% compared with that at 3 days, indicating that an increased effect of PP on D_{eff} as the hydration age progressed in a fixed water content system. In Case II, difference between the maximum and minimum D_{eff} values at 3 and 56 days was 4.7 and 0.3 $m^2 \cdot s^{-1}$, respectively. As the hydration age increased, the difference in D_{eff} values decreased. A similar trend can be observed in Case III, as shown in Fig. 24c. The results indicated the influence of PP on D_{eff} would decrease as the hydration age increased for hydration systems with a fixed C_3S content or with a fixed w/s ratio. Previous study (L. Liu et al., 2020a, 2020b) has demonstrated that the hydration kinetics and microstructure development of C_3S paste at early ages of hydration can be significantly affected by the particle shape, attributed to variations in specific surface area and geometry. However, at later ages, the geometric attributes of cement particles have less impact on pore parameters. In Cases II and III, the effect of PIP on D_{eff} exhibited a resemblance to the influence of particle shape on D_{eff} in hydration systems. This similarity arises from the fact that PIP significantly modifies the specific surface area of C_3S particles during hydration when sealed pores transition into open pores.

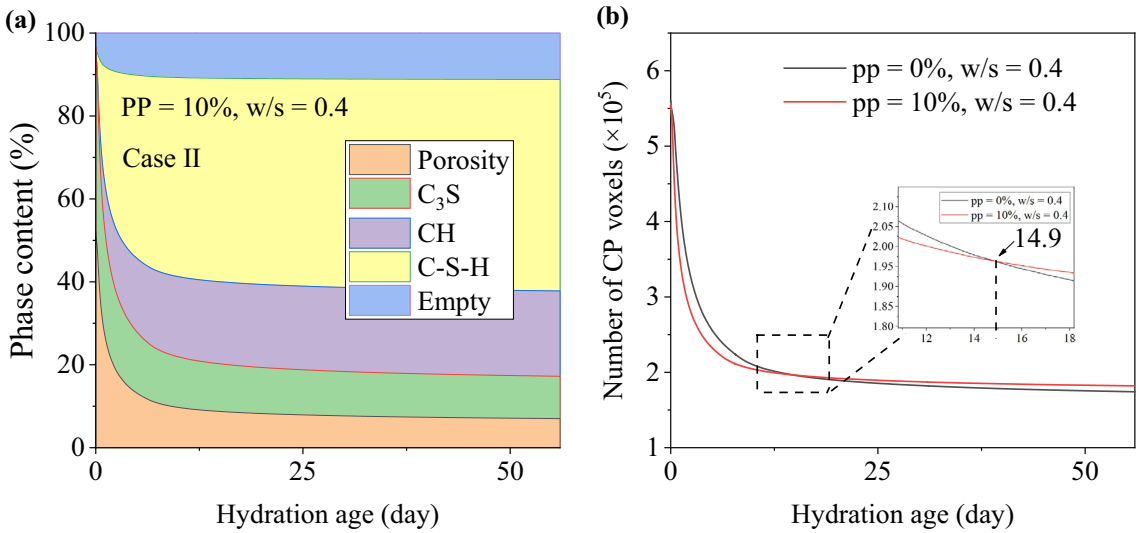

Fig. 21 Evolution of phase contents and number of CP voxels obtained from Case II: (**a**) Phase contents obtained with PP of 10%; (**b**) Number of CP voxels

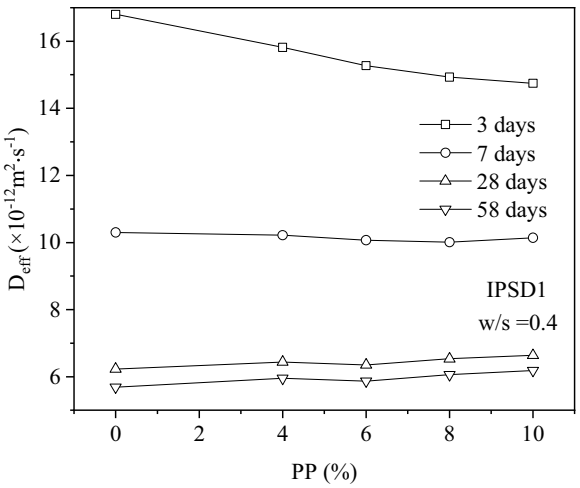

Fig. 22 D_{eff} obtained from Case III with different PPs at w/s = 0.4

4.4 Effect of Water-to-Solid Ratio

Figure 25a–d show the evolution of D_{eff} values obtained from Case I at various w/s ratios. In Case I, the PIP was constructed by removing certain C_3S voxels from the RVE. The water content was kept constant across different RVEs. Therefore, w/s ratio would slightly increase with the increase of PP value. The w/s ratio for the RVE with a PP of 0% was defined as the initial w/s ratio.

In Fig. 25a, the D_{eff} values obtained at 3 days exhibited an increase as initial w/s ratio increased. The discreteness of D_{eff} was evaluated using the coefficient of variation (CV) (Shen et al., 2022; Wu et al., 2020a). For an initial w/s ratio of 0.4, 0.5 and 0.6, the CV for D_{eff} was 1.42%, 0.7% and 0.37%, respectively, at 3 days. These results indicated that the w/s ratio did not have much influence on the discreteness of D_{eff} in Case I during the early ages of hydration. However, as hydration proceeded, the influence of w/s ratio on the discreteness of D_{eff} increased. This trend is evident in Table 4, where the average CV for the effective diffusion coefficients at 7, 28, and 56 days, was 4.2%, 7.9%, and 8.7%, respectively. The CV value increased with hydration age. Nevertheless, no simple relationship can be established between the discreteness of D_{eff} obtained at different PPs and w/s ratios when hydration age was the same, as shown in Table 4.

Figure 26 shows the evolution of D_{eff} values obtained from Case II with different w/s ratios. In Case II, the C_3S content was kept constant across simulations by adding extra C_3S voxels to the RVEs. Therefore, the w/s ratio for RVEs would slightly decrease as PP value increased. In Fig. 26, the effective diffusion coefficients exhibited an increase with the rise in the w/s ratio when PP and hydration age were kept constant. The average CVs for the effective diffusion coefficients obtained at 3, 7, 28, and 56 days with different PPs is shown in Table 5. The CV values were 9.5%, 7.1%, 3.4%, and 2.9%, respectively. These results indicated that the discreteness of D_{eff} for different PPs decreased as the hydration age increased in Case II.

At 3 days, the CV for effective diffusion coefficients decreased from 11.61% to 7.73% when the initial w/s ratio increased from 0.4 to 0.6. Similar trends were observed for the effective diffusion coefficients obtained at 7 days in Fig. 26b. However, the CV for the effective

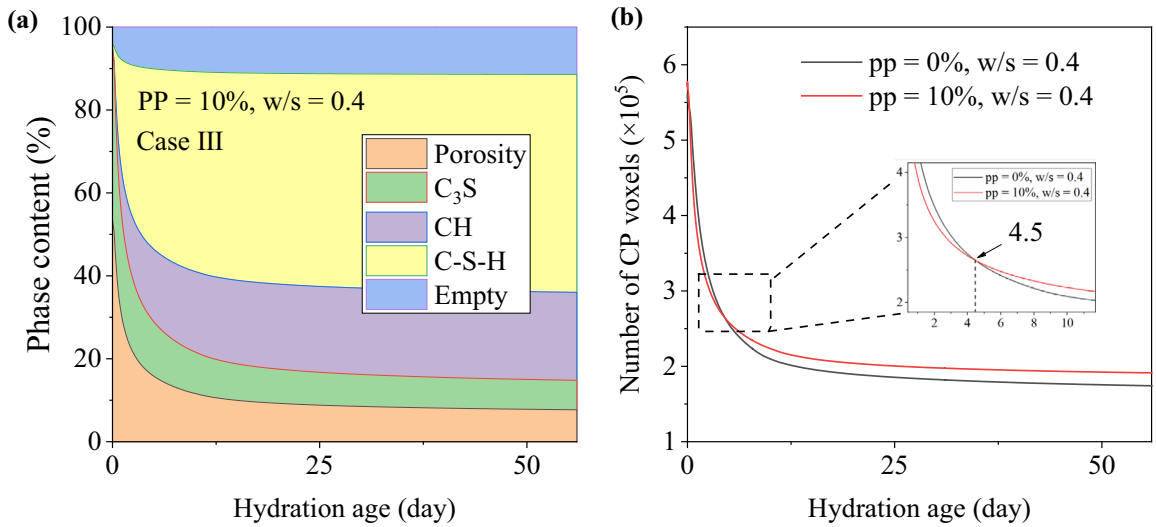

Fig. 23 Evolution of phase contents and number of CP voxels obtained from Case III: (**a**) Phase contents obtained with PP of 10%; (**b**) Number of CP voxels

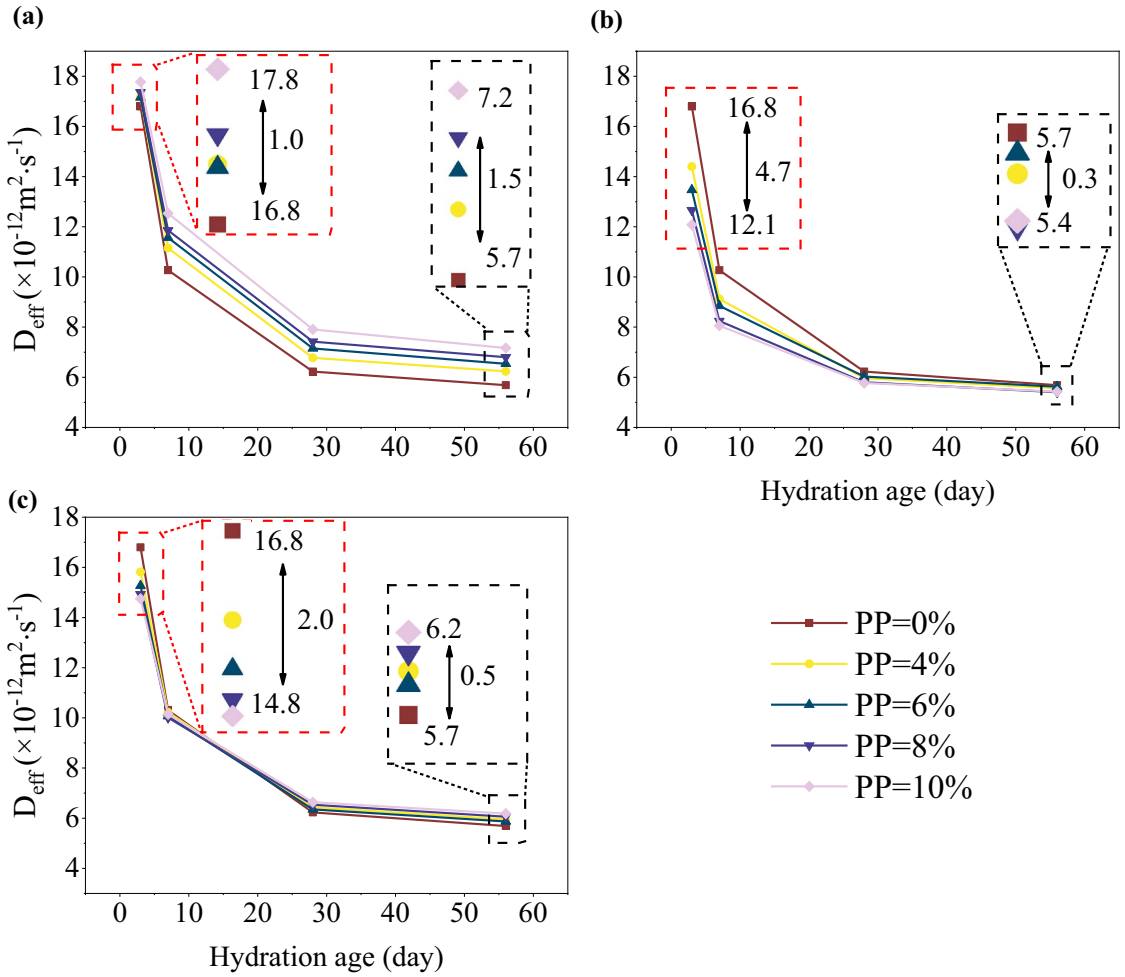

Fig. 24 D_{eff} obtained with different hydration age at initial w/s = 0.4: (**a**) Case I; (**b**) Case II; (**c**) Case III

diffusion coefficients at 28 and 56 days did not exhibit a decreasing trend with an increase in the initial w/s ratio. These results suggested that the discreteness of effective diffusion coefficients for different PPs decreased as the w/s ratio increased during the early ages of hydration (less than 28 days) when the C_3S content was kept constant across simulations. However, no simple relationship was observed between w/s ratio and the discreteness of effective diffusion coefficients during the later ages of hydration (28 days or more).

Figure 27a–d show the evolution of D_{eff} obtained from Case III with different w/s ratios. In Fig. 27, the D_{eff} increased with the increase of w/s ratio regardless of hydration age and PPs. The CV for D_{eff} obtained with different PPs at 3 days increased from 4.72 to 4.87% where w/s ratio increased from 0.4 to 0.5, as shown in Table 6. Similar results were also observed in the simulation when hydration age was 7 days. The results indicated that the discreteness of D_{eff} obtained at early ages of hydration (< 28 days) would increase as w/s ratio increased in Case III. However, the CV of D_{eff} obtained at 28 and 56 days did not show a decreasing trend. The result indicated that there was no simple relationship between the discreteness of effective diffusion coefficients and w/s ratios at late ages of hydration in Case III.

5 Conclusions

This study analyzed the effects of PIPs on the ionic diffusivity of hydrated C_3S paste through hydration-diffusion simulations. The major conclusions can be summarized as follows:

(1) A hydration-diffusion method considering the effects of PIPs was proposed to estimate the ionic diffusivity of hydrated C_3S paste. In this method, the algorithm of original CEMHYD3D model was upgraded to incorporate the effects of

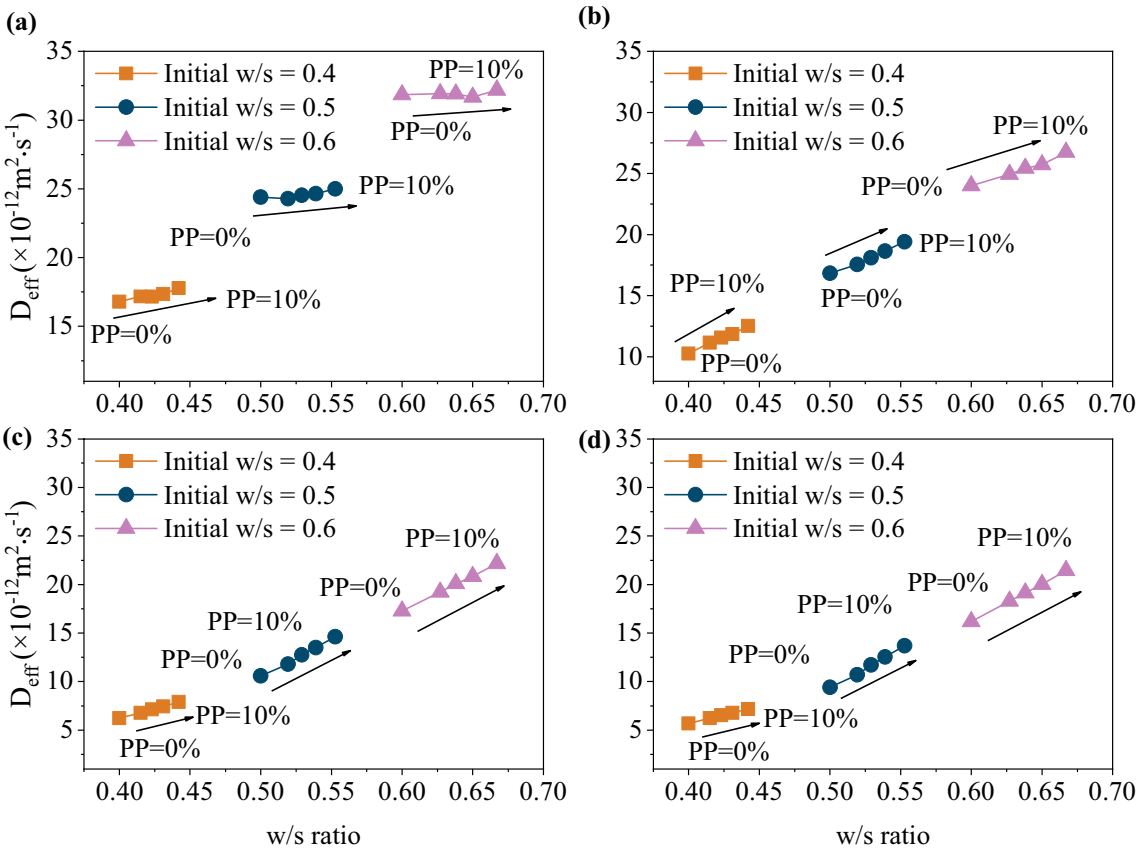

Fig. 25 Effective diffusion coefficient obtained from Case I with different w/s ratios: (**a**) 3 days; (**b**) 7 days; (**c**) 28 days; (**d**) 56 days

Table 4 The value of CV for D_{eff} obtained from Case I

Hydration age (days)	Initial w/s ratio	CV (%)	Average CV (%)
3	0.4	1.42	0.8
	0.5	0.70	
	0.6	0.37	
7	0.4	5.70	4.2
	0.5	4.15	
	0.6	2.89	
28	0.4	6.92	7.9
	0.5	9.49	
	0.6	7.28	
56	0.4	6.89	8.7
	0.5	11.02	
	0.6	8.19	

PIP size distributions and PP. Then, the modified CEMHYD3D model was combined with the FEM model to simulate the steady-state ionic diffusion. The proposed method was validated using data from electro-migration experiments.

(2) The effect of PIP size distribution was dependent on the water content, C_3S content, and w/s ratio in the hydration systems. The hydration system with a wider PIP size distribution would obtain a higher ionic diffusivity compared with a narrower one when the water content in the RVEs was kept constant. In this case, the difference in effective diffusion coefficient between wide and narrow PIP size distributions decreased as the hydration age increased. In Case II, the standard deviation for ΔD_{eff} at 3, 7, 28, and 56 days was determined as 12.5×10^{-5}, 6.16×10^{-5}, 7.80×10^{-5},

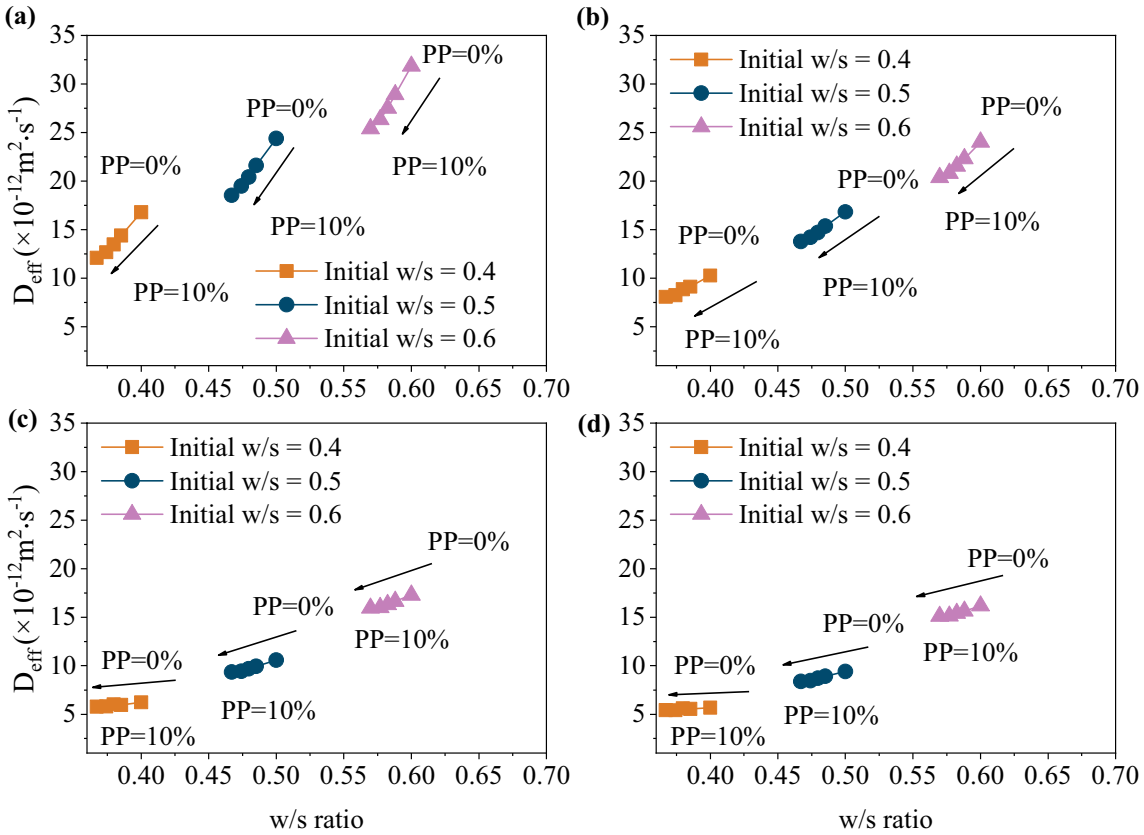

Fig. 26 Effective diffusion coefficients obtained from Case II with different w/s ratios: (**a**) 3 days; (**b**) 7 days; (**c**) 28 days; (**d**) 56 days

Table 5 The value of CV for effective diffusion coefficients obtained from Case II

Hydration age (days)	Initial w/s ratio	CV (%)	Average CV (%)
3	0.4	11.61	9.5
	0.5	9.28	
	0.6	7.73	
7	0.4	8.61	7.1
	0.5	6.90	
	0.6	5.71	
28	0.4	2.71	3.4
	0.5	4.53	
	0.6	2.96	
56	0.4	1.94	2.9
	0.5	4.18	
	0.6	2.54	

and 6.83×10^{-5}, respectively. Therefore, for hydration systems with a fixed C_3S content, at early ages, the difference in ionic diffusivity induced by PIP size distribution exhibited a decreasing trend as hydration age increased. At later ages, this difference did not exhibit a significant decrease. The findings of Case II are also valid for Case III.

(3) The effect of PP on the ionic diffusivity in C_3S paste was dependent on water content, C_3S content, w/s ratio, and hydration age. For hydration systems with a fixed water content, an increase in PP would lead to an increase in the effective diffusion coefficient. In Case II, the D_{eff} at 3 days with a PP of 10% was 28% lower than that with a PP of 0% at the same hydration age. These results indicate that, at early ages, for hydration systems with a fixed C_3S content, higher PP leads to lower ionic diffusivity compared to lower PP. This conclusion also holds for Case III.

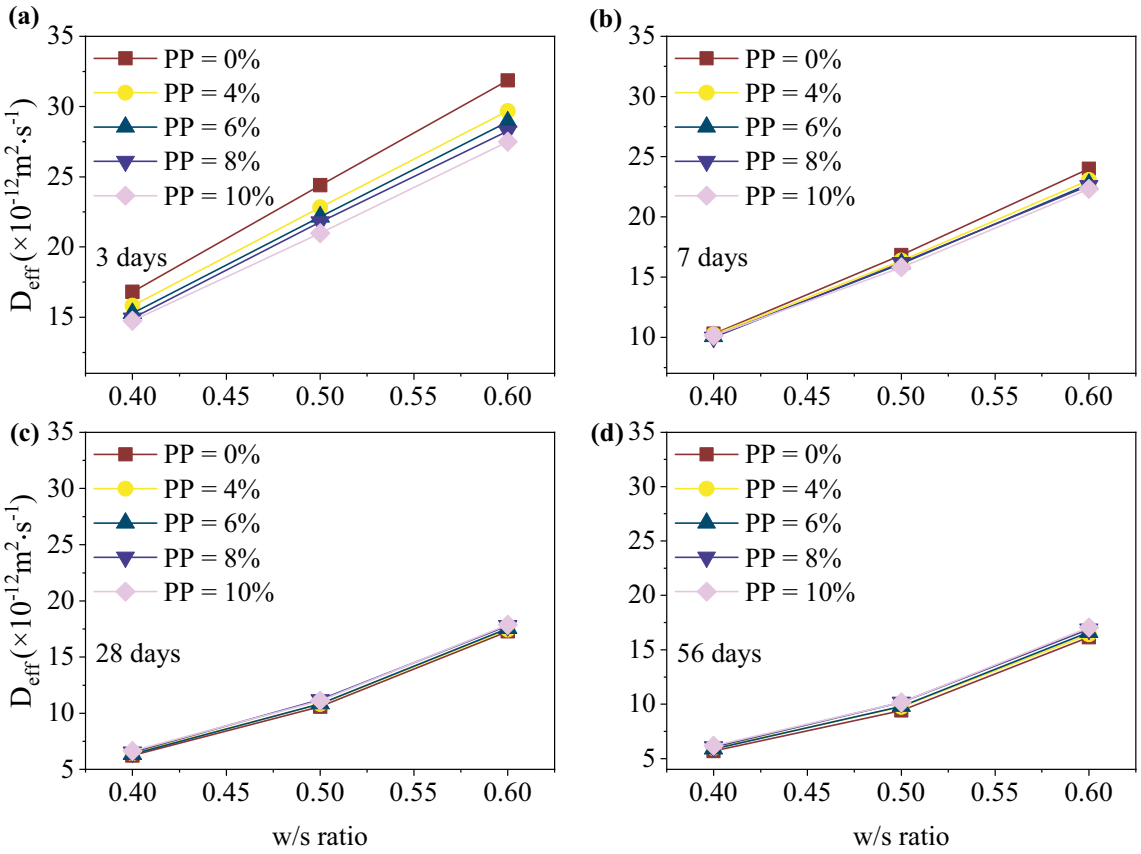

Fig. 27 Effective diffusion coefficient obtained from Case III with different w/s ratios: (**a**) 3 days; (**b**) 7 days; (**c**) 28 days; (**d**) 56 days

Table 6 The value of CV for D_{eff} obtained from Case III

Hydration age (days)	Initial w/s ratio	CV (%)	Average CV (%)
3	0.4	4.72	4.79
	0.5	4.77	
	0.6	4.87	
7	0.4	1.14	1.83
	0.5	1.85	
	0.6	2.50	
28	0.4	1.94	1.72
	0.5	2.12	
	0.6	1.12	
56	0.4	2.47	2.34
	0.5	2.84	
	0.6	1.72	

(4) The low CVs observed for D_{eff} at 3 days (1.42%, 0.7%, and 0.37% for w/s ratios of 0.4, 0.5, and 0.6, respectively) demonstrate that, for the conditions in Case I, the initial w/s ratio has a negligible effect on the effective diffusion coefficient during early hydration, independent of the PP values. However, this influence would increase at later ages. There was no simple relationship between the discreteness of effective diffusion coefficients and w/s ratios at later ages of hydration.

6 Limitations of this Study

The macroscopic voids within the C_3S paste were not considered in the simulation due to the constrained RVE size. In the future work, the influence of these voids would be investigated through more computationally efficient simulation techniques, such as a multiscale modeling approach. The second limitation of the present study was that the PP and IPSD employed in the simulation were approximate values.

Acknowledgements
Not applicable.

Author contributions
XW: conceptualization, methodology, data curation, writing–original draft, funding acquisition. DS: conceptualization, review and editing. ST: review

and editing, data curation, investigation. RL: data curation, investigation. All authors read and approved the final manuscript.

Funding
The authors gratefully acknowledge the Natural Science Foundation of Jiangsu Province (Grant No. BK20241529), and China Postdoctoral Science Foundation (Grant No. 2024M750736).

Availability of data and materials
The data sets used for the current study are available from the corresponding authors on reasonable request.

Declarations

Competing interests
The authors declare no competing interests.

Received: 21 October 2024 Accepted: 2 March 2025
Published online: 07 June 2025

References

Andrade, C. (1993). Calculation of chloride diffusion coefficients in concrete from ionic migration measurements. *Cement and Concrete Research, 23*(3), 724–742. https://doi.org/10.1016/0008-8846(93)90023-3

ASCE. (2019). *Report card for America's infrastructure; American Society of Civil Engineers, Reston, United States,* http://www.infrastructurereportcard.org/. American Society of Civil Engineers.

Bakharev, T., Sanjayan, J. G., & Cheng, Y. B. (2002). Sulfate attack on alkali-activated slag concrete. *Cement and Concrete Research, 32*(2), 211–216. https://doi.org/10.1016/S0008-8846(01)00659-7

Barnes, P., & Bensted, J. (2003). *Structure and performance of cements*. CRC Press.

Bejaoui, S., & Bary, B. (2007). Modeling of the link between microstructure and effective diffusivity of cement pastes using a simplified composite model. *Cement and Concrete Research, 37*(3), 469–480. https://doi.org/10.1016/j.cemconres.2006.06.004

Bellmann, F., Sowoidnich, T., Ludwig, H. M., & Damidot, D. (2012). Analysis of the surface of tricalcium silicate during the induction period by X-ray photoelectron spectroscopy. *Cement and Concrete Research, 42*(9), 1189–1198. https://doi.org/10.1016/j.cemconres.2012.05.011

Bentz, D. P. (2000). *CEMHYD3D: A three-dimensional cement hydration and microstructure development modeling package. Version 2.0* (Report 6485, Issue.

Bentz, D. P. (2005). *CEMHYD3D: A three-dimensional cement hydration and microstructure development modeling package. Version 3.0* (Report 7232[R], Issue.

Bernard, F., & Kamali-Bernard, S. (2010). Performance simulation and quantitative analysis of cement-based materials subjected to leaching. *Computational Materials Science, 50*(1), 218–226. https://doi.org/10.1016/j.commatsci.2010.08.002

Bernard, F., & Kamali-Bernard, S. (2012). Predicting the evolution of mechanical and diffusivity properties of cement pastes and mortars for various hydration degrees—a numerical simulation investigation. *Computational Materials Science, 61*, 106–115. https://doi.org/10.1016/j.commatsci.2012.03.023

Biernacki, J. J., & Gottapu, M. (2015). An advanced single-particle model for C_3S hydration—validating the statistical independence of model parameters. *Computers and Concrete, 15*(6), 898–999. https://doi.org/10.1298/cac.2015.15.6.989

Bullard, J. W. (2008). A determination of hydration mechanisms for tricalcium silicate using a kinetic cellular automaton model. *Journal of the American Ceramic Society, 91*(7), 2088–2097. https://doi.org/10.1111/j.1551-2916.2008.02419.x

Carrara, P., De Lorenzis, L., & Bentz, D. P. (2016). Chloride diffusivity in hardened cement paste from microscale analyses and accounting for binding effects. *Modelling and Simulation in Materials Science and Engineering, 24*(6), 065009. https://doi.org/10.1088/0965-0393/24/6/065009

Chen, B., Lin, W., Liu, X., Iacoviello, F., Shearing, P., & Robinson, I. (2019). Pore structure development during hydration of tricalcium silicate by X-ray nano-imaging in three dimensions. *Construction and Building Materials, 200*, 318–323. https://doi.org/10.1016/j.conbuildmat.2018.12.120

Cheng, X. (2022). *Research of multi-ion transport mechanism and ionic reaction behavior in the concrete under the electric field*. Zhejiang University.

Costoya Fernández, M. M. (2008). *Effect of particle size on the hydration kinetics and microstructural development of tricalcium silicate*. EPFL.

Do, H. Q., Bishnoi, S., & Scrivener, K. L. (2015). Microstructural modelling of the elastic properties of tricalcium silicate pastes at early ages. *Computers and Concrete, 16*(1), 125–140. https://doi.org/10.1298/cac.2015.16.1.125

Dridi, W. (2013). Analysis of effective diffusivity of cement based materials by multi-scale modelling. *Materials and Structures, 46*(1), 313–326. https://doi.org/10.1617/s11527-012-9903-5

Gospodinov, P., Mironova, M., & Kazandjiev, R. (2007). Mechanisms of sulfate ionic diffusion in porous cement based composites. *Computers and Concrete, 4*(4), 273–284. https://doi.org/10.1298/cac.2007.4.4.273

Ismail, I., Bernal, S. A., Provis, J. L., Hamdan, S., & van Deventer, J. S. J. (2013). Microstructural changes in alkali activated fly ash/slag geopolymers with sulfate exposure. *Materials and Structures, 46*(3), 361–373. https://doi.org/10.1617/s11527-012-9906-2

Kurdowski, W. (2014). *Cement and concrete chemistry*. Springer.

Liu, C., Huang, R., Zhang, Y. S., Liu, Z. Y., & Zhang, M. Z. (2018a). Modelling of irregular-shaped cement particles and microstructural development of Portland cement. *Construction and Building Materials, 168*, 362–378. https://doi.org/10.1016/j.conbuildmat.2018.02.142

Liu, C., Liu, G. J., Liu, Z. Y., Yang, L., Zhang, M. Z., & Zhang, Y. S. (2018b). Numerical simulation of the effect of cement particle shapes on capillary pore structures in hardened cement pastes. *Construction and Building Materials, 173*, 615–628. https://doi.org/10.1016/j.conbuildmat.2018.04.039

Liu, C., Wang, F. Z., & Zhang, M. Z. (2020a). Modelling of 3D microstructure and effective diffusivity of fly ash blended cement paste. *Cement and Concrete Composites, 110*, 103586. https://doi.org/10.1016/j.conbuildmat.2018.02.142

Liu, C., & Zhang, M. Z. (2021). Effect of curing temperature on hydration, microstructure and ionic diffusivity of fly ash blended cement paste: A modelling study. *Construction and Building Materials, 297*, 123834. https://doi.org/10.1016/j.conbuildmat.2021.123834

Liu, L., Tao, G., Chen, H., & Zhu, Z. (2020b). Shape effect of cement particles on the ionic diffusivity of hardened cement paste—a three-dimensional numerical investigation. *Construction and Building Materials, 250*, 118736. https://doi.org/10.1016/j.conbuildmat.2020.118736

Mehta, P. K., & Monteiro, P. J. M. (2007). *Concrete microstructure properties and materials*. McGraw-Hill Education.

Mien, T. V., Stitmannaithum, B., & Nawa, T. (2011). Prediction of chloride diffusion coefficient of concrete under flexural cyclic load. *Computers and Concrete, 8*(3), 343–355. https://doi.org/10.1298/cac.2011.8.3.343

Neville, A. (2004). The confused world of sulfate attack on concrete. *Cement and Concrete Research, 34*(8), 1275–1296. https://doi.org/10.1016/j.cemconres.2004.04.004

Ngala, V. T., Page, C. L., Parrott, L. J., & Yu, S. W. (1995). Diffusion in cementitious materials: II, further investigations of chloride and oxygen diffusion in well-cured OPC and OPC/30%PFA pastes. *Cement and Concrete Research, 25*(4), 819–826. https://doi.org/10.1016/0008-8846(95)00072-K

Oh, B. H., & Jang, S. Y. (2004). Prediction of diffusivity of concrete based on simple analytic equations. *Cement and Concrete Research, 34*(3), 463–480. https://doi.org/10.1016/j.cemconres.2003.08.026

Patel, R. A., Perko, J., Jacques, D., De Schutter, G., Ye, G., & Van Bruegel, K. (2018). Effective diffusivity of cement pastes from virtual microstructures: Role of gel porosity and capillary pore percolation. *Construction and Building Materials, 165*, 833–845. https://doi.org/10.1016/j.conbuildmat.2018.01.010

Patel, R. A., Phung, Q. T., Seetharam, S. C., Perko, J., Jacques, D., Maes, N., De Schutter, G., Ye, G., & Van Breugel, K. (2016). Diffusivity of saturated ordinary Portland cement-based materials: A critical review of experimental and analytical modelling approaches. *Cement and Concrete Research, 90*, 52–72. https://doi.org/10.1016/j.cemconres.2016.09.015

Poupard, O., Ait-Mokhtar, A., & Dumargue, P. (2004). Corrosion by chlorides in reinforced concrete: Determination of chloride concentration threshold by impedance spectroscopy. *Cement and Concrete Research, 34*(6), 991–1000. https://doi.org/10.1016/j.cemconres.2003.11.009

Scrivener, K. L., Juilland, P., & Monteiro, P. J. M. (2015). Advances in understanding hydration of Portland cement. *Cement and Concrete Research, 78*, 38–56. https://doi.org/10.1016/j.cemconres.2015.05.025
Scrivener, K. L., Ouzia, A., Juilland, P., & Kunhi Mohamed, A. (2019). Advances in understanding cement hydration mechanisms. *Cement and Concrete Research, 124*, 105823. https://doi.org/10.1016/j.cemconres.2019.105823
Shen, D., & Wang, X. (2023). *Simulation on hydration of tricalcium silicate in cement clinker*. Springer.
Shen, D., Wang, X., & Wu, S. (2022). Determining hydration mechanisms for initial fall and main hydration peak in tricalcium silicate hydration using a two-scale hydration simulation model. *Cement and Concrete Research, 156*, 106763. https://doi.org/10.1016/j.cemconres.2022.106763
Shi, X., Xie, N., Fortune, K., & Gong, J. (2012). Durability of steel reinforced concrete in chloride environments: An overview. *Construction and Building Materials, 30*, 125–138. https://doi.org/10.1016/j.conbuildmat.2011.12.038
Tang, L. (1996). *Chloride transport in concrete -measurement and prediction*. Chalmers University of Technology.
Tang, L. (1999a). Concentration dependence of diffusion and migration of chloride ions: Part 1. Theoretical considerations. *Cement and Concrete Research, 29*(9), 1463–1468. https://doi.org/10.1016/S0008-8846(99)00121-0
Tang, L. (1999b). Concentration dependence of diffusion and migration of chloride ions: Part 2. Experimental evaluations. *Cement and Concrete Research, 29*(9), 1469–1474. https://doi.org/10.1016/S0008-8846(99)00120-9
Tao, G. (2020). *Multi-scale modeling on the chloride diffusion in cement-based materials[D]*. Hohai University.
Taylor, H. F. W. (1997). *Cement chemistry*. Thomas Telford.
Thepaper. (2022). *Technology pathway for low carbonisation of concrete; China Building Materials, Beijing, China*. https://m.thepaper.cn/baijiahao_19461963. China Building Materials News.
Wang, X. Y., Park, K. B., & Lee, H. S. (2012). Modeling of chloride diffusion in a hydrating concrete incorporating silica fume. *Computers and Concrete, 10*(5), 523–539. https://doi.org/10.1298/cac.2012.10.5.523
Wang, X., Shen, D., Tao, S., Liu, R., & Wu, S. (2025). Estimation of chloride diffusivity in hydrated tricalcium silicate using a hydration-diffusion integrated method. *Journal of Wuhan University of Technology-Mater Sci Ed, 40*(1), 49–64. https://doi.org/10.1007/s11595-025-3040-9
Wang, X., Shen, D., & Wu, S. (2021). Influence of particle internal pores on hydration kinetics and microstructure development in tricalcium silicate hydration. *Journal of Materials in Civil Engineering, 33*(12), 04021335. https://doi.org/10.1061/(ASCE)MT.1943-5533.0003963
Wilson, W., Georget, F., & Scrivener, K. (2021). Unravelling chloride transport/microstructure relationships for blended-cement pastes with the mini-migration method. *Cement and Concrete Research, 140*, 106264. https://doi.org/10.1016/j.cemconres.2020.106264
Wu, S., Wang, X., Shen, D., Sun, K., & Zhu, J. (2020a). Simulation analysis on hydration kinetics and microstructure development of tricalcium silicate considering dissolution mechanisms. *Construction and Building Materials, 249*, 118535. https://doi.org/10.1016/j.conbuildmat.2020.118535
Wu, S., Wang, X., Shen, D., Sun, K., & Zhu, J. (2020b). Simulations of diffusion-controlled and dissolution mechanisms with respect to the deceleration period of tricalcium silicate hydration. *Construction and Building Materials, 265*, 120458. https://doi.org/10.1016/j.conbuildmat.2020.120458
Xie, T., & Biernacki, J. J. (2011). The origins and evolution of cement hydration models. *Computers and Concrete, 8*(6), 647–675. https://doi.org/10.1298/cac.2011.8.6.647
Yang, F., Liu, X. P., Zhao, Y. J., Zhang, Y. M., Wang, P. M., Robinson, I., & Chen, B. (2018). Investigation of three-dimensional microstructure of tricalcium Silicate (C_3S) by electron microscopy. *Materials, 11*(7), 1110–1119. https://doi.org/10.3390/ma11071110
Zhang, M. (2013). *Multiscale lattice Boltzmann-finite element modelling of transport properties in cement-based materials[D]*. Delft University of Technology.
Zhang, Y., Liu, C., Liu, Z., Liu, G., & Yang, L. (2017). Modelling of diffusion behavior of ions in low-density and high-density calcium silicate hydrate. *Construction and Building Materials, 155*, 965–980. https://doi.org/10.1016/j.conbuildmat.2017.08.128
Zhang, Y., Luzio, G. D., & Alnaggar, M. (2021). Coupled multi-physics simulation of chloride diffusion in saturated and unsaturated concrete. *Construction and Building Materials, 292*, 123394. https://doi.org/10.1016/j.conbuildmat.2021.123394
Zhu, Z., Xu, W., Chen, H., & Tan, Z. (2020). Evolution of microstructures of cement paste via continuous-based hydration model of non-spherical cement particles. *Composites Part b: Engineering, 185*, 107795. https://doi.org/10.1016/j.compositesb.2020.107795
Zhu, Z. G., Xu, W. X., Chen, H. S., Wang, Y., Gou, X. F., Liu, L., & Gu, Y. (2021). Diffusivity of cement paste via a continuum-based microstructure and hydration model: Influence of cement grain shape. *Cement and Concrete Composites, 118*, 103920. https://doi.org/10.1016/j.cemconcomp.2020.103920

Publisher's Note

Xin Wang is a postdoctoral researcher at Hohai University. His research focuses on cement hydration mechanisms, multiscale simulation of cement-based materials, and durability assessment of concrete structures. He has published multiple studies on microstructure-property relationships in the field of cement research.

Dejian Shen is a professor at Hohai University, where he earned his BS and MS degrees. He obtained his PhD from Tongji University (Shanghai, China). His research spans computational materials science, early-age cracking control in concrete, seismic design of industrial structures, and FRP-based rehabilitation of reinforced concrete.

Sijie Tao is a PhD student at Hohai University. Her research interests include molecular dynamics simulation, quantum chemical and density functional theory calculation of cementitious materials. She has published articles in the field of molecular dynamics simulation.

Ruixin Liu is a PhD student at Hohai University. His research interests include quantum chemical and density functional theory calculation.